ELSEVIER

Fusion Engineering and Design 38 (1997) 27–57

Fusion Engineering and Design

Physics basis for a reversed shear tokamak power plant

S.C. Jardin [a], C.E. Kessel [a,*], C.G. Bathke [b], D.A. Ehst [c], T.K. Mau [d], F. Najmabadi [d], T.W. Petrie [e], The ARIES Team

[a] *Princeton Plasma Physics Laboratory, P.O. Box 451, Princeton, NJ 08543, USA*
[b] *Los Alamos National Laboratory, P.O. Box 1663, Los Alamos, NM 87545, USA*
[c] *Argonne National Laboratory, 9700 S. Cass Avenue, Argonne, IL 60439, USA*
[d] *Fusion Energy Research Program, University of California, San Diego, 9500 Gilman Drive, La Jolla, CA 92093, USA*
[e] *General Atomics, P.O. Box 85608, San Diego, CA 92186, USA*

Abstract

The reversed shear plasma configuration is examined as the basis for a tokamak fusion power plant. Analysis of plasma equilibrium and ideal MHD stability, bootstrap current and current drive, plasma vertical stability and position control, divertor physics and plasma power balance are used to determine the operating point parameters that maximize fusion power density and minimize the recirculating power fraction. The final plasma configuration for the ARIES-RS power plant obtains β of 4.96%, plasma driven current fraction of 91%, plasma current of 11.3 MA, toroidal field of 8.0 T and major and minor radius of 5.5 and 1.4 m. The current drive system utilizes fast wave, lower hybrid and high frequency fast wave current drive to obtain maximum current profile flexibility, requiring ≤ 80 MW of power. A divertor solution is found which employs neon impurity injection to enhance the radiation in the scrape-off layer (SOL) and divertor and results in a combined particle and heat load in the divertor of ≤ 6 MW m^{-2}. The plasma is driven with a Q of 25 and is at a thermally stable operating point. The plasma is assumed to be in an ELMy H-mode, with low amplitude and high frequency ELMs.

Keywords: Reversed shear; Tokamak power plant; Plasma configuration

1. Introduction

The reversed shear plasma configuration has shown considerable potential for providing the basis of an economically competitive fusion power plant. The benefits of this configuration are that it achieves both high β_N and high β, it obtains large bootstrap current fractions with very good current profile alignment and appears to provide the transport suppression necessary to sustain the pressure profile that is consistent with high β and high bootstrap current [1,2]. The primary characteristics of a reversed shear plasma are a hollow current profile, a non-monotonic safety factor profile and relatively peaked pressure profiles. The hollow current gives rise to the safety factor profile, which initially decreases from its value at the plasma center to a minimum value and then rises from there to its value at the plasma edge. It

* Corresponding author. Tel.: +1 609 2432294; fax: +1 609 2432111; e-mail: ckessel@pppl.gov

0920-3796/97/$17.00
PII S0920-3796(97)00111-7

is the initial decrease in the safety factor that provides negative magnetic shear, which is responsible for stability to $n = \infty$ ballooning modes and suppression of plasma transport. The name 'reversed shear' arises from the fact that the safety factor in a conventional tokamak plasma rises monotonically from the plasma center to the edge.

Like all configurations with β_N values which exceed the first stability regime this plasma requires a conducting wall to stabilize low-n external kink modes. For ballooning modes the reversed shear plasma obtains second stability in the region inside the minimum safety factor and first stability outside this region. However, what distinguishes it from other high β_N second stability plasma configurations is that it obtains high plasma current simultaneously with high central safety factor. This is achieved by using a hollow current profile. Typical second stability plasmas must reduce plasma current (to raise the safety factor) to obtain high β_N, only allowing β to weakly increase over first stability values. An additional advantage of the reverse shear configuration is that the hollow current profile matches very closely with the natural shape of the plasma generated bootstrap current profile. This allows one to significantly reduce the amount of external current drive required.

Recent experiments [3–5] have demonstrated transiently the improved MHD stability and suppression of plasma particle and energy transport. Complete demonstration of all the favorable properties simultaneously will require steady state conditions, which are not accessible in present experimental devices. Some earlier experiments [6–8] demonstrated the existence of non-monotonic safety factor profiles, however, these had minimum q values around 1.0 causing internal instabilities to dominate the discharge behavior. More interesting is that each of these was produced by different means; elongation and current ramping in DIII-D, pellet injection in JET and lower hybrid current drive in Tore Supra. All experiments observed varying degrees of influence on the plasma energy and/or particle transport.

After theoretical predictions indicated transport, ideal MHD stability and bootstrap/current drive advantages of the reversed shear configuration with $q > 2$ everywhere in the plasma, experiments on several devices were performed to examine this regime. Both TFTR and DIII-D utilized similar approaches with special timing of plasma current ramps and heating to inductively produce the non-monotonic q-profiles. These discharges are transient, with the current profile continuously diffusing, which eventually causes the negative magnetic shear to disappear. Both experiments were outfitted with the motional stark effect diagnostic [9], that allows accurate reconstruction of the safety factor profile which was absent in the earlier experiments mentioned above.

In TFTR the typical configuration had safety factor values of $q_0 \approx 3$–4, $q_{\min} \geq 2$ and minimum position of $r_{\min}/a \approx 0.3$. The peak ion temperature reached 24 keV while the electrons reached 10 keV. The central electron density increased by a factor of three up to 1.2×10^{20} m^{-3}. The resulting pressure profile had a peak to volume average of eight, which even exceeds the value of five which is typical of TFTR's high confinement mode called supershot. The changes in the temperature and density profiles after the reversed shear configuration has formed indicate very significant reductions in the energy and particle diffusivities. For TFTR the plasma rotation is small due to balanced neutral beam injection.

In DIII-D the typical configuration had safety factor values of $q_0 \approx 6$, $q_{\min} \geq 2$ and minimum position of $r_{\min}/a \approx 0.5$. The peak ion temperature reached 22 keV while the electrons obtained 6 keV. The central electron density increased by a factor of two up to 6.0×10^{19} m^{-3}. The pressure profile had a peak to volume average of five. The plasma rotation was strong in DIII-D with rotation frequencies of 60 kHz, since all the neutral beams are oriented in the same direction. In addition, the shear in the plasma rotation was very steep in the vicinity of $q_{\min}$. DIII-D also produced these configurations in both L-mode and H-mode.

Both experiments have determined that the plasma core is in the second stability regime for ballooning modes. In addition, both experiments obtain β limits consistent with ideal MHD stability predictions and these are expected to be responsible for the discharge terminations. Some of

the reverse shear discharges in DIII-D indicate that a resistive mode may be responsible for the discharge termination. The global energy confinement times obtained in these experiments have H-factors over ITER89-P scaling of 2–3. In addition, bootstrap current fractions between 50 and 75% have been calculated. It should be noted that in addition to the bulk plasma rotation produced by neutral beams in these discharges, there is considerable toroidal plasma rotation associated with the strong pressure gradient set up by the transport barrier. It is presently an area of research to understand the importance of this plasma rotation and its shear for transport and MHD stability.

Very recently, efforts to produce steady state reverse shear plasmas with lower hybrid current drive have been reported by Tore Supra [10] and JT-60U [11]. Tore Supra injected 2.5 MW of lower hybrid power and drove 50% of the plasma current, with the lower hybrid (LH) current centered about an r/a of 0.4. The negative magnetic shear was maintained for over 4 s. The plasma stored energy and peak electron temperature increased by 1.6 soon after the LH power was injected and the reverse shear safety factor profile established. Faraday rotation measurements were used to determine the safety factor profile. The experiments on JT-60U formed an ohmic reversed shear plasma and then injected lower hybrid current drive to maintain it. The shear reversal point started at an r/a of 0.6 and relaxed to 0.5. The inductive current is estimated to be between 25–40% of the total plasma current. The motional stark effect diagnostic was employed to determine the safety factor profile. The reversed shear configuration was held in steady state for 4 s. Neither experiments found evidence for any MHD activity, although the β values were not high.

2. MHD stability and bootstrap current

Several reversed shear equilibria were examined to assess the balance between maximizing β (fusion power) and minimizing the external current drive (recirculating power). The plasma equilibria are determined using a fixed boundary flux coordinate equilibrium calculation. Ideal MHD stability calculations are carried out for $n = \infty$ ballooning modes and $n = 1$–4 external kink modes. A conducting wall placed at 0.3 times the minor radius measured from the plasma boundary was used in most of the parameter scans, although the reference configuration value ended up at 0.095. Several examinations were made to determine the impact of plasma aspect ratio, triangularity, elongation, pressure and current profiles and the kink stabilizing wall position and these are reported in the following.

The bootstrap current is calculated using the full Hirshman–Sigmar expression with a velocity space representation of the viscosity coefficients [12]. The bootstrap current profile can be roughly given by $j_{bs} \propto -\sqrt{\epsilon} R(dp/d\psi)$, which shows that the pressure gradient profile dominantly determines the bootstrap current shape. This is an important consideration when searching for MHD stable equilibria. The bootstrap current profile is naturally hollow, which provides for very good profile alignment with the reversed shear current profile required for MHD stability.

The plasma particle and energy transport are not explicitly modelled. Once a stable plasma equilibrium is found, the plasma temperature is adjusted to provide the largest and best aligned bootstrap current profile. Since it is predicted and experimentally observed, that a transport barrier exists in the region of the minimum safety factor, efforts are made to restrict the location of the dominant gradients of the temperature and density inside of this vicinity.

The reference plasma configuration for the ARIES-RS power plant is given in Fig. 1 and Table 1. The sections that follow will demonstrate the analysis done to define the physics tradeoffs that determined the reference configuration. It should be noted that the operating β value is reduced to 90% of the maximum stable value to provide some margin to the stability boundary.

2.1. Plasma pressure and current profiles

The equilibria studied here are determined by specifying the pressure and parallel current

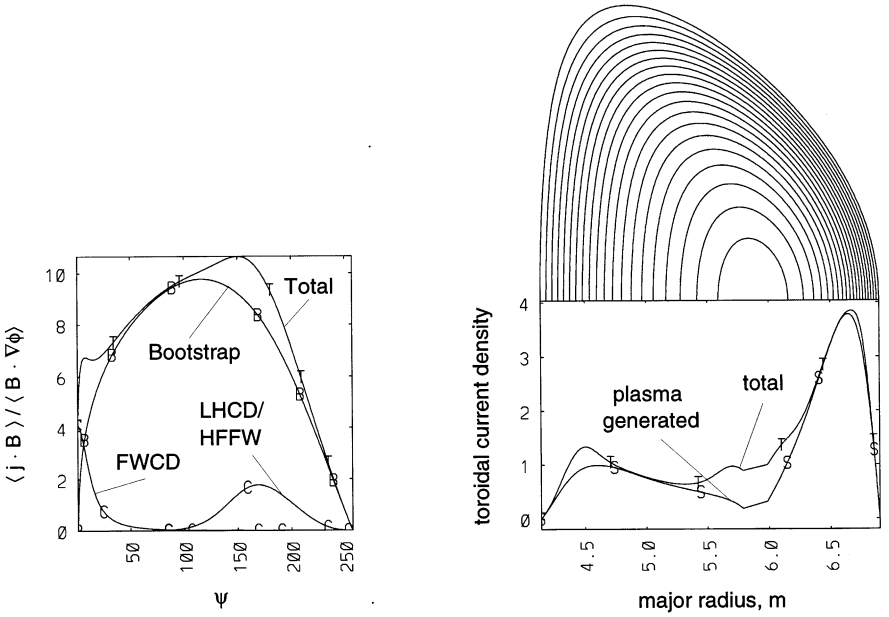

Fig. 1. The reference plasma equilibrium parallel current profile as a function of poloidal flux, the plasma flux surface contours, and toroidal current density as a function of the major radius.

profile, along with the plasma boundary and toroidal field strength.

The plasma parallel current profile is given by,

$$\frac{\langle j \cdot B \rangle}{\langle B \cdot \nabla \phi \rangle} = j_0(1-\hat{\psi}) + j_1 \frac{d^2(1-\hat{\psi})^2\hat{\psi}}{(\hat{\psi}-\psi_0)^2 + d^2} \quad (1)$$

Here $\hat{\psi} = (\psi - \psi_{\text{axis}})/(\psi_{\text{edge}} - \psi_{\text{axis}})$ and d has the value 0.25. The current profile is chosen to place the minimum in the safety factor as far out as possible while keeping the edge safety factor between 3.5 and 4.0. This moves the low-n kink mode structure closer to the stabilizing conducting wall. The minimum can not be moved too close to the plasma boundary, or there will be insufficient magnetic shear to stabilize the external kink modes even in the presence of a conducting wall. In addition, the central safety factor is chosen to provide a sufficient degree of negative magnetic shear, roughly given by $q_0 - q_{\min} \geq 0.3$. For all cases $q_{\min}$ is kept above 2.0 and q_0 is kept below 3.0 to avoid multiple integral safety factor values, which serves as a crude method to avoid resistive instabilities. These current profiles resulted in $\hat{\psi}(q_{\min})$ positions of between 0.6 and 0.7, while the $q_{\min}$ values varied from 2.2 to 2.6. Experimental values for $\hat{\psi}(q_{\min})$ range from 0.1 to 0.4, although these are obtained inductively in transient discharges without external current drive to control the current profile. Moving the location of the $q_{\min}$ as far out as possible also allows the pressure gradient to be moved closer to the plasma boundary. This can provide improved bootstrap current alignment without significantly reducing the maximum stable β.

The pressure profile has a very strong impact on both the MHD stability and the bootstrap current alignment. The pressure profile used in this study is given by:

$$p = p_0(1-\hat{\psi}^{\alpha})^{2.0} \quad (2)$$

The exponent α is varied from 1.0 to 1.8 to examine the impact of broadness. From the scan of plasma pressure profiles the maximum β decreased as the pressure profile was broadened (as alpha was increased), however, this led to the bootstrap current peaking further from the plasma center and improved bootstrap current profile alignment. Since the position of the minimum in the safety factor is fixed at its maximum distance from the plasma center, as the plasma

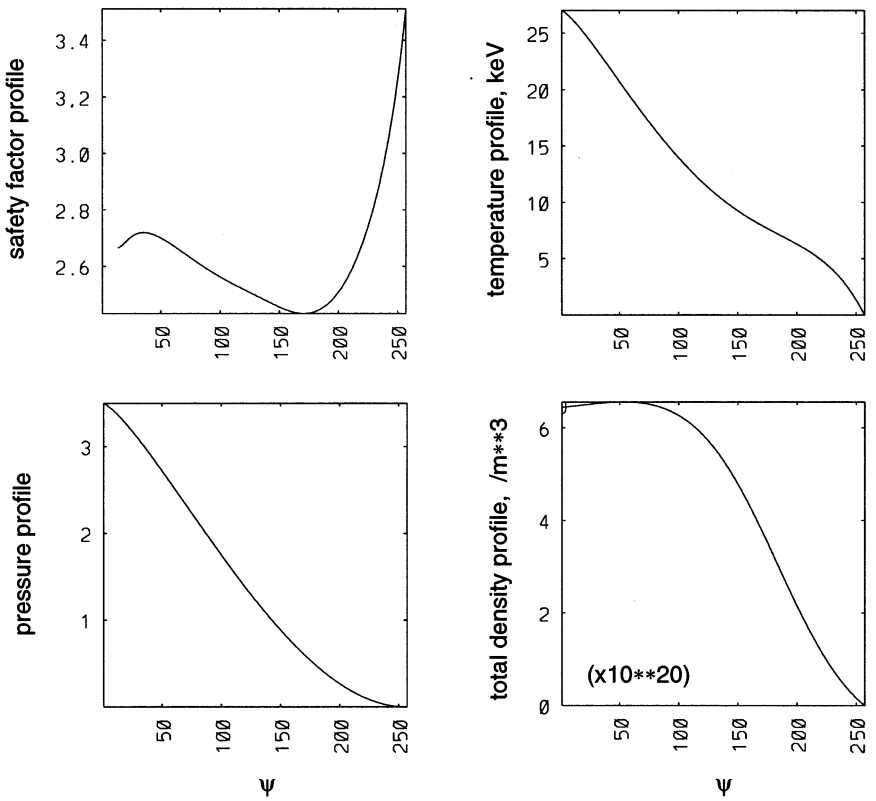

Fig. 2. The reference plasma equilibrium profiles for the safety factor, pressure, temperature and density as a function of poloidal flux.

pressure profile is broadened the pressure gradient is moved further out. Consequently, the $n = \infty$ ballooning modes become the limiting instability. As the pressure profile is made more peaked, with the conducting shell at 0.3, the low-n kink modes become the limiting instability (in particular, $n = 3$). The presence of the stabilizing wall only affects the low-n kink modes. This results in the highest β limits being obtained with peaked pressure profiles. However, these produce bootstrap current near the plasma center, where we are trying to maintain a hollow current profile. Thus, these high β limits can not be realized because of bootstrap limitations. The very broadest pressure profiles produce the best bootstrap current alignment with the desired current profile, however, their β limits are significantly lower and we are unable to obtain bootstrap fractions approaching unity. In addition, because these are limited by the $n = \infty$ ballooning modes, they are not affected by the conducting wall.

The best tradeoff between these considerations led to the pressure profile exponent range (α) of 1.3–1.4 at all aspect ratios and leads to the $n = \infty$ ballooning and low-n kink stability limits to lie near each other, along with providing excellent bootstrap current alignment. The value of the pressure exponent is fixed for all subsequent calculations at either 1.3 or 1.4. The results of the pressure profile scan for a 95% flux surface elongation of 1.7, triangularity of 0.5 and aspect ratio 4.0, are given in Table 2.

2.2. Aspect ratio

In order to limit the parameter space for subsequent calculations the aspect ratio scan was done first. Four aspect ratios were examined; 3.0, 3.5,

Table 1
Reference reversed shear plasma configuration

I_p (MA)	11.32
B_T (T)	7.98
R (m)	5.52
a (m)	1.38
κ (95%)	1.70
δ (95%)	0.50
β_p	2.28
β (%)	4.96
β^* (%)	6.18
β_N (%)	4.83
β_N^{max} (%)	5.35
q_0 (axis)	2.80
q_{min} (minimum)	2.49
$\hat{\psi}$ (q_{min})	0.69
q_e (edge)	3.52
I_{bs} (MA)	10.0
$I_{\nabla p}/I_p$	0.91
I_{CD} (MA)	1.15
q_*	2.37
$l_i(3)$	0.42
$n_0/\langle n\rangle$	1.36
$T_0/\langle T\rangle$	1.98
$p_0/\langle p\rangle$	2.20
Kink wall	0.095

4.0 and 4.5. In each case the maximum stable β is found and the bootstrap current is maximized, subject to the constraints on temperature and density profiles mentioned in Section 2. The results are presented in Table 3.

The β_N values increased as the aspect ratio decreased. This combined with the increase in total plasma current at fixed q_* causes the β to increase faster than β_N. The resulting plasma driven current, which includes bootstrap, diamagnetic and Phirsch–Schluter currents, exceeds 89%

Table 2
Variation of β with pressure profile exponent

α	β_N^{max}	β^{max}	$f_{\nabla p}$	I_{CD} (MA)
1.20[a]	5.77	5.95	0.78	2.28
1.30	5.35	5.54	0.89	1.20
1.40	5.00	5.17	0.89	1.19
1.50[b]	4.64	4.80	0.87	1.37
1.60[b]	4.36	4.50	0.87	1.36

[a] Bootstrap limited, $f_{\nabla p}$ and I_{CD} correspond to $\beta_N = 4.6$ and $\beta = 4.74$.
[b] $T(\psi)$ and $n(\psi)$ do not obey transport constraints.

Table 3
Optimized plasma equilibria with varying aspect ratio

	$A = 3.0$	$A = 3.5$	$A = 4.0$	$A = 4.5$
R (m)	5.40	5.40	5.40	5.40
a (m)	1.80	1.54	1.35	1.21
κ (95%)	1.80	1.80	1.80	1.80
δ (95%)	0.50	0.50	0.50	0.50
β_p	1.75	1.95	2.05	2.16
β^{max} (%)	8.29	6.83	5.46	4.50
β_N^{max} (%)	5.50	5.30	4.85	4.50
q_0 (axis)	2.88	2.88	2.70	2.50
q_e (edge)	3.88	3.61	3.47	3.46
q_{min} (minimum)	2.62	2.51	2.39	2.18
q_*	2.35	2.35	2.35	2.35
$l_i(3)$	0.39	0.41	0.43	0.48
$\hat{\psi}$ (q_{min})	0.66	0.68	0.68	0.58
$I_{\nabla p}/I_p$	0.90	0.90	0.89	0.92
I_{CD} (MA)	1.80	1.50	1.40	0.95
Kink wall	0.30	0.30	0.30	0.30

in all cases. As the aspect ratio decreased the amount of off-axis current drive required increased. Although values are reported for the required current drive in Table 3, these are from equilibrium calculations and detailed current drive calculations are necessary to determine these accurately. This is reported in Section 3. From a combination of systems analysis and engineering the aspect ratio was set at 4.0 and this will be used for all subsequent investigations.

2.3. Plasma shape

The plasma shape has a strong impact on the MHD stability. In particular, the plasma triangularity provides benefits for $n = \infty$ ballooning modes by enhancing the good curvature along a magnetic field line and for low-n external kink modes by enhancing the global magnetic shear at the plasma edge. This latter point is especially important for reversed shear equilibria because moving the minimum in the safety factor closer to the plasma boundary tends to reduce magnetic shear there. Even though a conducting wall is used to aid in stabilizing low-n external kink modes, sufficient shear in the plasma must still be present to obtain full stabilization. A scan of the maximum achievable β_N as a function of the

plasma triangularity, ranging from 0.2 to 0.6, showed that β_N dropped precipitously below a triangularity of 0.4 and rose at a significant, but slower rate above this value. These calculations were made with a fixed elongation of 1.8, the aspect ratio was 4.0, the conducting wall at $0.3a$ and the safety factor at the plasma edge was held at approximately 3.5. Since the edge safety factor was held fixed during the scan, the plasma current decreased (or q_* increased) as the triangularity decreased. Therefore, the β would be reduced by more than simply the reduction in β_N, due to the scaling $\beta \propto \beta_N/q_*$. The opposite holds true as the triangularity is increased and β shows a consistent increase over the entire range. These results are given in Table 4. The triangularity is limited by the ability to design a divertor for the inboard separatrix that allows sufficient neutron shielding. The 95% triangularity is taken to be 0.5 for the reference configuration.

The plasma elongation also provides significant benefits for β, both from increased plasma current and increased magnetic shear. However, since elongating the plasma makes it vertically unstable, the elongation is limited to allow conducting structures and feedback control systems to be designed. The conducting structure surrounding the plasma is designed to provide a safety margin, defined as $f_s = 1 + \tau_g/\tau_{L/R}$ of 1.2. This safety margin represents the margin to ideal instability where the plasma is uncontrollable and occurs when $f_s = 1.0$. The time constants τ_g and $\tau_{L/R}$ are the plasma vertical growth time and the structure eddy current L/R time. The distance of the conducting structure from the plasma boundary and its poloidal extent are determined to meet this criteria. Once this is established then the resistivity and thickness of the structure are chosen to allow for a reasonable feedback control power. From vertical stability and dynamic control simulations the required structure on the outboard extends from 55 to 90° at 0.5 times the minor radius measured from the plasma boundary. The inboard structure extends from 135 to 145° at 0.35 times the minor radius. Both of these structures reside in the gap between the reflector and shield. The plasma elongation at the separatrix (and the 95% flux surface) was reduced from 2.0 to 1.9 (1.8–1.7) to allow the structure to be moved into the reflector to shield gap. The structures are made of tungsten, 4 cm thick and are made electrically continuous in the toroidal direction. The control requirement is to provide for a 1 cm RMS random disturbance with time scale equal to the plasma vertical growth time. If the feedback control coils are located in the gap between the reflector and shield on the outboard side a peak power of 15 MVA is required. If the feedback control coils are located behind the shield on the outboard side, the peak power is 40 MVA. A large fraction of the feedback control power is reactive, which indicates that they can be recovered with proper power supply and energy storage design. Therefore, these powers do not have to be continuously supplied as part of the recirculating power.

Table 4
Variation of β with triangularity at $A = 4.0$

δ	β_N^{max}	β^{max}	q_*	I_p (MA)
0.20	2.15	2.00	2.85	8.95
0.30	3.20	3.13	2.69	9.47
0.40	4.30	4.60	2.48	10.3
0.50	4.85	5.45	2.35	10.8
0.60	5.15	6.25	2.18	11.7

2.4. Conducting shell and plasma rotation for low-n kink modes

It is important to emphasize that a conducting wall is required for these configurations to obtain the high β values. Since no second stability regime has been found for the low-n kink modes, as there is for the $n = \infty$ ballooning modes [13,14], it is necessary to utilize a conducting wall to access the higher pressures where a fusion power plant can become significantly more attractive. Recent experiments [15] and theory [16] indicate that a resistive wall can stabilize the low-n kink modes if plasma rotation and a dissipation mechanism in the plasma are present. The reversed shear configuration can better utilize a wall than a plasma with a monotonic safety factor profile. This arises because of the presence of the zero

magnetic shear ($dq/d\psi = 0$) region which causes the kink mode structure to shift to that vicinity. If the zero shear region is moved closer to the plasma edge, one moves the plasma displacements associated with the instability closer to the conducting wall, thereby making the wall more effective at suppressing them. In the absence of a conducting wall, the reversed shear plasmas typically obtain similar or lower β values as compared to plasmas with monotonic safety factor profiles. From theoretical analysis one can approximate the requirements to stabilize the low-n kink modes. The plasma must rotate at about 5–10% of the Alfven speed, resulting in a $2.8–5.6 \times 10^5$ m s^{-1} rotation speed. The actual conducting wall should be located at the ideal wall position for the plasma mode to provide the greatest margin to the resistive wall mode, which occurs when the wall is too close to the plasma. It is the ideal wall position that is referred to in this report. The wall has conductivity and thickness requirements that are given by $\Delta/\eta > 1.5 \times 10^4$, where Δ is the wall thickness and η is the resistivity.

The effectiveness of a conducting wall for suppressing the ideal external kink modes is presently an active area of research and the actual rotation requirements are quite uncertain. Recent theoretical estimates by Boozer [17] indicate that the plasma rotation required may be significantly less than that predicted so far. The basis for this theory appears to address the fact that the resistive wall mode, the unstable mode that arises when the ideal plasma mode is stabilized by a non-perfectly conducting wall, grows on a much longer time-scale than the original ideal instability. This time-scale is sufficiently long for the finite resistivity and 3D nature of the plasma to allow an island to develop from this initially 2D ideal instability. Once an island can form the stabilization from plasma rotation is the same as that for resistive tearing modes [18], which requires considerably slower plasma rotation speeds to suppress the growth of the instability. More extensive experimental analysis is required to determine the necessary rotation speeds.

Since plasma rotation is a necessary component for stabilization of low-n external kink modes, the means for providing this rotation must be addressed. Most present tokamak experiments have neutral beam injection for heating and depending on the beam orientation, it can provide large toroidal rotation speeds ($1–5 \times 10^5$ m s^{-1}). However, most fusion power plant studies utilize RF heating and current drive. Toroidal rotation speeds from ICH [19–21] indicate values up to 3×10^4 m s^{-1}, which arises from pumping out of the fast ions created by the waves, giving rise to an $E_r \times B$ rotation. A recent report [22] indicates that excitation of electrostatic kinetic Alfven waves directly imparts toroidal momentum to the plasma, giving toroidal rotation speeds of 6×10^3 m s^{-1}. Whether these RF driven plasma rotation speeds will be sufficient for kink mode stabilization is not clear, however, the speeds observed so far in experiments fall between the two theoretical estimates.

Scans were also performed to examine the impact of a conducting wall located closer to the plasma than for the 0.3 case used in the scans. This was done at the aspect ratio 4.0. For wall positions of 0.25 or less the plasma stability was limited by ballooning modes, since the closer wall significantly raised the stability limit for low-n kink modes. A more peaked pressure profile can raise the ballooning stability limit and take advantage of the increased low-n kink stability limit. However, the peaking of the pressure profile leads to bootstrap current closer to the plasma center. For these more peaked pressure profiles, in order to avoid bootstrap current overdrive, the β_N is restricted to lie below some value, resulting in reduced total bootstrap current and worse alignment. The ballooning modes are the limiting constraint for medium to broad pressure profiles. The results indicate that the highest β_N possible, in conjunction with a bootstrap fraction that is $\geq 90\%$, can be no larger than about 5.35, for a conducting wall closer than or equal to 0.25. This corresponds to the aspect ratio of 4.0, along with an elongation of 1.7 and triangularity of 0.5 at the 95% flux surface. The corresponding maximum β_N for the slightly higher elongation of 1.8 is 5.6.

It was found that integrating the conducting wall for kink stabilization as part of the blanket structure already present was the best solution. The final wall position is located at 0.095 times

the minor radius measured from the plasma edge. This wall is part of the vanadium structure in the blanket, it is 2 cm thick and is only required to extend from -85 to $+85$ degrees in the poloidal direction on the outboard side. This structure is not toroidally continuous.

3. Current drive

3.1. General considerations

In a typical reversed shear configuration, it is possible to obtain very good alignment between the equilibrium and bootstrap current profiles [1]. In the ARIES-RS reference equilibrium, the plasma driven current fraction is 0.91, using density and temperature profiles which are characteristic of reversed shear plasmas. External noninductive techniques are generally required to drive seed currents at the plasma center and off axis near the shear reversal region.

The analysis described in this section is aimed at determining the current drive (CD) requirements for steady state operation at the desired conditions. First, the noninductive techniques most suitable for driving currents in the various plasma regions will be identified. The CD requirements will then consist of the power delivered to the plasma and specific conditions for launching the power. In the case of radio-frequency techniques, these conditions may include the wave frequency, the wave spectrum characterized by its peak refractive index along the magnetic field, $N_{\|}$ and the wave launcher location. It is noted that the total CD power requirement and the projected wall-plug-to-plasma recirculating power and its cost of electricity.

To assess the current drive power requirement, a combination of selected CD techniques will be used to drive the seed currents in the different regions of the plasma. In principle, self-consistent calculations that match the driven current profile to that of the target plasma equilibrium are necessary to obtain accurate estimates of the current drive power. Another analytical approach which seeks an optimal match of the driven current profile to the target seed current profile has also been used. The latter method proves particularly useful in providing a set of CD efficiency scalings with plasma and machine parameters that are suitable for power plant systems analysis. Both of these analytical treatments of current drive will be discussed in the following subsections and results on the CD requirements will be described.

3.2. Current drive techniques

A number of noninductive current-drive techniques have been considered for the reversed shear (RS) power plant. Depending on the reference equilibrium, a combination of these techniques are required to drive currents in different locations within the plasma. The bulk of the present experimental database on current drive has been obtained using LH waves and neutral beams (NB). These experiments were mostly carried out in transient L-mode discharges, where the bootstrap current is a small fraction of the total current ($f_{BS} \leq 0.1$). There are two other CD techniques, namely, fast magnetosonic waves in the ion cyclotron range of frequencies (ICRF) and electron cyclotron (EC) waves, that have some experimental data and exhibit potentials for power plant applications. The fast wave (FW) technique shows significant promise for on-axis current drive, particularly in view of the fact that a typical fusion plasma core is inaccessible to the LH waves. In previous studies [23,24], RF waves were used as the reference CD technique, based on physics, engineering and cost considerations. Following the same reasoning, current drive in this study will also be focused on RF techniques.

Because of their natural tendency to propagate radially towards the plasma center, ICRF fast waves are most suitable for current drive on the magnetic axis. On the other hand, with a proper launched spectrum, the LH wave can be made to drive currents on the outer parts of the plasma. However, the choice of an RF technique for off-axis (between axis and edge) current drive is not as straightforward. Several candidates have been considered, including high-frequency fast waves (HFFW), mode conversion current drive, minority heating current drive and EC waves. These techniques all have the potential capability

of localized off-axis current drive in a fusion plasma core, each using a distinct physical mechanism. But they are all in early stages of development so that a definitive selection among them is not warranted at this point.

For our ARIES-RS design, we will focus on HFFW as the reference technique for off-axis current generation, but recognize that there may be equally attractive candidates that have not been fully explored in this study. Indeed, seeking the most attractive technique to drive currents off-axis in the plasma core is presently a topic of intense research interest.

The physics basis for HFFW current drive is as follows. The operational frequency is in the range of the 20th ion cyclotron harmonic. The technique relies on the total absorption of the wave energy by electrons well before it reaches the magnetic axis. The success of this method depends on the high electron beta of the plasma and the avoidance of mode conversion to the slow wave and to the ion Bernstein wave at the cyclotron harmonics beyond the antenna coupling region. Earlier HFFW experiments [25] (e.g. JIPPT-IIU, JFT-2M, PLT) all indicated results very similar to those of LH waves and led to the conclusion that mode conversion of the fast wave to the slow branch did occur in these experiments. It can be argued that in a fusion plasma, the situation will be quite different. Because of the higher electron beta, larger plasma size and strong absorption by energetic alphas near the magnetic axis, the wave will be completely damped in less than half a radial transit of the plasma, as predicted by ray tracing calculations shown in this section. Thus, with a suitable launched $N_{\|}$-spectrum, the toroidal effects on propagation and the wave scattering process due to ambient density fluctuations, two main factors contributing to mode conversion to the slow branch, are expected to be minimized. As shown recently [26], mode conversion to the ion Bernstein branch and direct ion damping at the high harmonics will be negligible as long as the ion beta is less than about 30%, which is easily satisfied in a typical RS reactor plasma. Consequently, the fast wave can penetrate deeper to the fusion plasma core than the LH wave and drive currents closer to the magnetic axis. It is encouraging to note that in the recent series of high-power fast wave experiments on DIII-D, direct electron heating has been observed at frequencies as high as the 10th ion cyclotron harmonic. The planned HFFW experiments on a high-β device such as NSTX should strengthen the data base for this technique.

3.3. Current drive requirements

The current drive requirements include the total power delivered to the plasma, the launched power spectrum from each of the wave launchers and the locations of the launching structures on the first wall. Among them, the power requirement is the most critical in determining the economic attractiveness of the overall power plant design. To this end, two approaches have been taken in assessing the required current-drive (CD) power. The first approach attempts to obtain an optimum match to the target equilibrium current-density profile with the sum of externally driven currents by RF waves and of the bootstrap current. The second approach uses the sum of externally driven and bootstrap currents to self-consistently arrive at an equilibrium (different from the target) that is MHD stable and maintains the relevant global features of the target equilibrium. The first method allows for quick estimates of the CD power requirement and is useful for parametric studies; however it is not totally self-consistent since the externally driven currents computed will not exactly match those assumed when computing the original equilibrium. The second is self-consistent in this sense, but it requires time-consuming computations for convergence to a final equilibrium, which typically deviate from the initial desired equilibrium.

As such, the first approach has been used in determining scalings of the current-drive figure of merit, which is referred to as the bootstrap-aided normalized CD efficiency [27],

$$\gamma_B \equiv \bar{n}_{e,20} I_p(A) R(m) / P_{CD}(W) \tag{3}$$

to account for both the bootstrap current fraction and the intrinsic efficiency, γ_{CD}, of the CD techniques. Thus for f_{BS} not too close to unity, $\gamma_B \simeq \gamma_{CD}/(1-f_{BS})$. The γ_B scalings are calculated as a

function of volume-averaged electron temperature, $\bar{T}_e$ at various values of Z_{eff} and aspect ratio, A. This set of scalings is then used in the systems code to determine the optimum aspect ratio and operating parameters for the RS power plant.

3.3.1. Optimum fit approach

In this approach, three RF current-drive techniques are used with the reversed-shear configuration, namely, fast waves in the ion cyclotron range of frequencies for on-axis CD, high-frequency fast waves (in the 20th ion harmonic range) for off-axis core CD and lower hybrid waves for edge CD. The calculations are done using a ray tracing code, CURRAY [28], that has been benchmarked with fast-wave CD experiments on DIII-D. The major features of the code are:

- Fast and slow wave ray tracing from the ICRF to the LH range of frequencies;
- thermal ion and electron damping;
- energetic ion (or alpha) cyclotron damping based on a slowing down distribution function;
- two empirical scalings for the normalized CD efficiency;
- a bootstrap current model based on the Hirshman–Sigmar approach; and
- an algorithm for obtaining an optimum current profile match.

First, a stable equilibrium is obtained from the JSOLVER code, which has been adapted to a free-boundary EQDSK format for use with the CURRAY code. With a fixed pressure profile, the density and temperature profiles are adjusted to yield a bootstrap current density profile with the highest bootstrap fraction, f_{BS}. In this process, because of uncertainties with the kinetic alpha pressure profile and its contribution to the bootstrap current, it is assumed that the plasma pressure is made up entirely of thermal particles. This assumption also is in line with the systems code calculations. Care has also been taken to ensure that there is minimum or no bootstrap overdrive in the plasma interior (inside the RS region).

Next, a combination of RF antenna-like power spectra and their launch locations are selected so as to drive currents in their respective intended locations. The power distribution among the various launchers is then adjusted to arrive at an optimum current profile match. Let the subscripts 'eq' and 'dr' denote equilibrium and driven (RF + bootstrap) current density profiles, respectively and $\langle \cdot \rangle$ denote flux surface averages. An optimum match is reached when the ratio

$$\Re = \frac{\int dS |\langle \vec{j} \cdot \vec{B} \rangle_{eq} - \langle \vec{j} \cdot \vec{B} \rangle_{dr}| / \langle B \rangle}{\int dS |\langle \vec{j} \cdot \vec{B} \rangle_{eq}| / \langle B \rangle} \quad (4)$$

is a minimum, where $\int dS$ is the area integral over the minor cross section. Usually, the minimum value of $\Re$ is around 0.04 for a typical f_{BS} value of 0.88.

As an illustration, a case similar to the reference design point will be presented, with the following parameters: $R_0 = 5.12$ m, $A = 4.0$, $B_0 = 7.51$ T, $I_p = 10.8$ MA, $\beta = 5.85\%$, $q(0) = 2.82$ and $q(a) = 3.58$. The density and temperature profiles have been adjusted to eliminate bootstrap overdrive at the core: $n_{e0}/\bar{n}_e = 1.20$, $\bar{n}_e = 2.03 \times 10^{20}$ m^{-3}, $T_{e0}/\bar{T}_e = 2.15$, $\bar{T}_e = 16.5$ keV and $T_i/T_e = 0.9$. The ratio of separatrix-to-peak densities is fixed at $n_{ea}/n_{e0} = 0.2$ in order to satisfy the edge density pedestal constraint on the assumed ELMy H-mode RS discharge and to radiate part of the core heat flux in the scrape-off region away from the divertor plates. A trace vanadium impurity concentration of 0.1% is assumed in the plasma, which together with a 14% helium ash concentration and 50/50 DT fuel mixture gives an effective charge of $Z_{eff} = 1.69$. The fraction of energetic alpha pressure is 12% and the bootstrap current fraction is $f_{BS} = 0.82$.

The results of the current drive calculations using the optimum fit approach are shown in Fig. 3 and the RF power, frequency, launched $N_\parallel$ and launcher location for each current-drive system are given in Table 5. It is clear from the figure that the alignment between the driven and equilibrium current density profiles are not perfect, having a mismatch factor of $\Re \approx 0.04$. All three CD systems are required in this particular case, even though in some instances, only two or even one system may be sufficient, as will be shown below. All required wave spectra have values of $N_\parallel$ that can be launched by reasonable antenna designs. In this particular case study, the aggre-

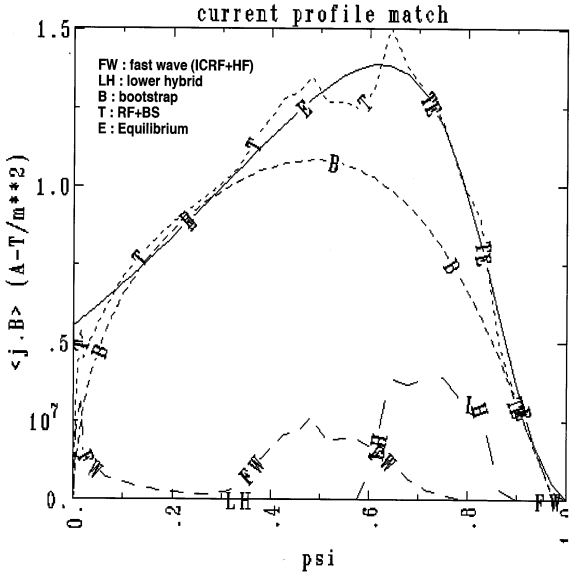

Fig. 3. Matching of the driven (RF + BS) current density profile to the target profile, using ICRF fast wave, HFFW and LH wave power, for a reversed shear equilibrium similar to the ARIES-RS design point.

gate CD efficiency is found to be $\gamma_B = 1.28 \times 10^{20}$ A W^{-1} m^{-2}.

In Fig. 4 the ray trajectories for the launched wave power are shown for the three RF systems. The rays are terminated when the power is completely absorbed. It is noted that for the ICRF rays, shown in Fig. 4, about 20% of the power is absorbed at the second tritium harmonic on the inboard side of the magnetic axis. For the launched HFFW power, 48 and 10% of the incident powers are absorbed by the energetic alpha particles along the $N_{\|} = 2.3$ and 2.5 rays, respectively. These trajectories also indicate that the HFFW power is absorbed completely in its initial radial transit, thus limiting the possibility of mode conversion to the slow wave. It is found that the locations of the launchers on the outboard side do not significantly impact the power deposition profile within the plasma, except in the case of ICRF fast waves.

3.3.2. Self-consistent approach

In this section, the self-consistent approach to calculate the current drive requirements is described. Recall that in a reversed shear (RS) equilibrium, a close match is possible between the bootstrap current profile and the desired current density profile of a high β stable equilibrium. Thus, for an accurate assessment, it is important to model the bootstrap current and the RF driven current accurately and in a manner self-consistent with the equilibrium, as will be shown.

The calculations treat the ions as multiple species, with the alpha particles given special consideration. Power balance calculations show the RS power plant will have a nonthermal ('fast') alpha pressure at the plasma center which is typical 10% of the total peak pressure. The fast alpha pressure, $p_{f\alpha}$, is strongly peaked on axis and decreases at lower temperatures, becoming negligible for $T_i \sim T_e \leq 5$ keV. Moreover, fast alpha spatial diffusion further lowers $p_{f\alpha}$ from classical thermalization on the local birth flux surface, so $p_{f\alpha}$ is typically 90% of the classical value. In the detailed bootstrap calculations, the thermal pressure profiles are given by reducing the total pressure by $p_{f\alpha}$:$p_{th} = p - p_{f\alpha}$. The temperature profiles for the various species are found by dividing the respective pressure profiles by the prescribed density profiles (that used in the equilibrium analysis). As a result the thermal species have temperature gradients depressed near the magnetic axis by the local peaking of the fast alpha pressure and the bootstrap contribution of the thermal species is likewise reduced. This effect is offset by the inclusion of the alphas (both thermal and nonthermal) with an effective temperature, $\bar{T}_\alpha$, given by $n_\alpha \bar{T}_\alpha = n_\alpha T_i + p_{f\alpha}$, where T_i is the fuel ion temperature and n_α is the alpha particle density.

Using this bootstrap model in the RIP ray tracing and MHD equilibrium code [24], a self-consistent calculation of the RS equilibrium with bootstrap and non-inductive seed current is achieved. A stable equilibrium at $A = 4.5$, provided by the JSOLVER code, was taken as an initial target. An ICRF fast wave antenna power distribution was found which provides fast-wave current drive (FWCD) that nearly duplicates the seed current profile of the target. The solution in RIP iterates between the MHD calculations of the equilibrium and the bootstrap/ray tracing on the resulting flux surfaces, which determines the cur-

Table 5
Current drive requirements for ARIES-RS-like equilibrium

CD system	Frequency (GHz)	$N_{\parallel}$	Power (MW)	Launcher site[a]
ICRF fast wave:	0.091	2.0	5.4	+15°
HF fast wave:	1.0	2.3	21.4	0°
	1.0	2.5	27.0	0°
LH wave:	4.6	1.9	9.5	−15°
	4.6	2.1	2.8	−15°
	3.5	2.3	6.4	+5°
	3.5	2.5	5.1	+5°
	3.5	3.0	10.5	+5°

[a] Degrees in poloidal angle above (+) or below (−) outboard midplane.

rent density profile for the equilibrium. The converged equilibrium was then tested by the PEST code, which confirmed MHD stability to ballooning and kink modes with a conducting wall located at $r = 1.3a$, a being the minor radius. The results of this set of calculations are displayed in Fig. 5.

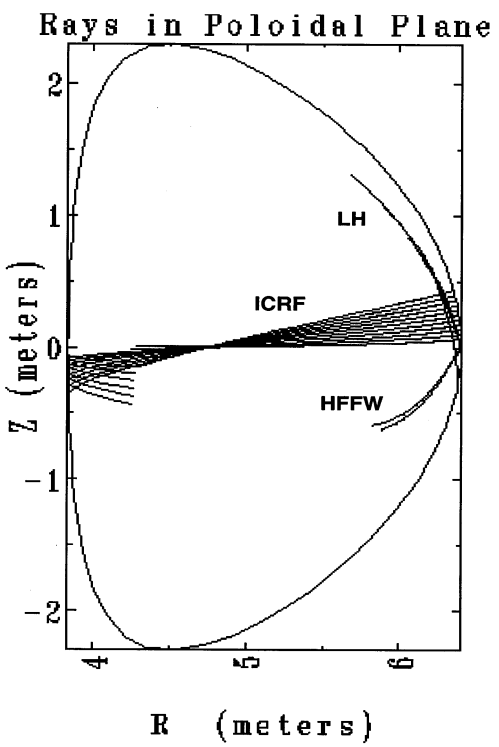

Fig. 4. Minor cross section view of the ray trajectories from the ICRF fast wave, HFFW, and LH wave launchers.

The pressure profile in this example is given by $p = p_0(1 - \hat{\psi}^{1.4})^2$, where $\hat{\psi}$ is the normalized poloidal flux (zero on axis). Note that the abscissa in the plots is Psihat $\equiv 1 - \hat{\psi}$. The density (solid) and temperature (dotted) profiles are shown in the lower left plot in Fig. 5. The upper center plot shows (chain-dash) $H = \langle \vec{j}_{BS} \cdot \vec{B} \rangle / \langle B^2 \rangle$, the bootstrap current profile, for the given temperature and density profiles, with $Z_{\text{eff}} = 1.34$ and $n_e/n_i = 1.16$. Also plotted is G, the FWCD portion, due to the array of antenna rays shown in the lower center plot. The total, $G + H$, is (solid curve) the stable equilibrium current density. Note that FWCD peaks near the magnetic axis, which is typical of FW damping at the location of peak plasma β. By careful adjustment of the poloidal distribution of the FW launched power, P_{FW}, the seed current profile can be tailored to provide the stable RS safety factor shown here at the lower right plot.

A desirable feature of this scenario is that only one driver technology is needed for these profiles and at this aspect ratio. Compared to LH or HFFW current drive, the ICRF fast wave system has the highest electrical efficiency and lowest unit cost. For the case illustrated ($B_0 = 7.07$ T, $R_0 = 5.99$ m), the selected frequency, 78 MHz (with $N_{\parallel} = 2.4$), places only the second tritium cyclotron harmonic at $R = 5.3$ m, on the inboard side of the magnetic axis. The strong electron damping results in only 12% of the launched power lost to tritium absorption and over 99% of the launched power is absorbed in the initial pass through the

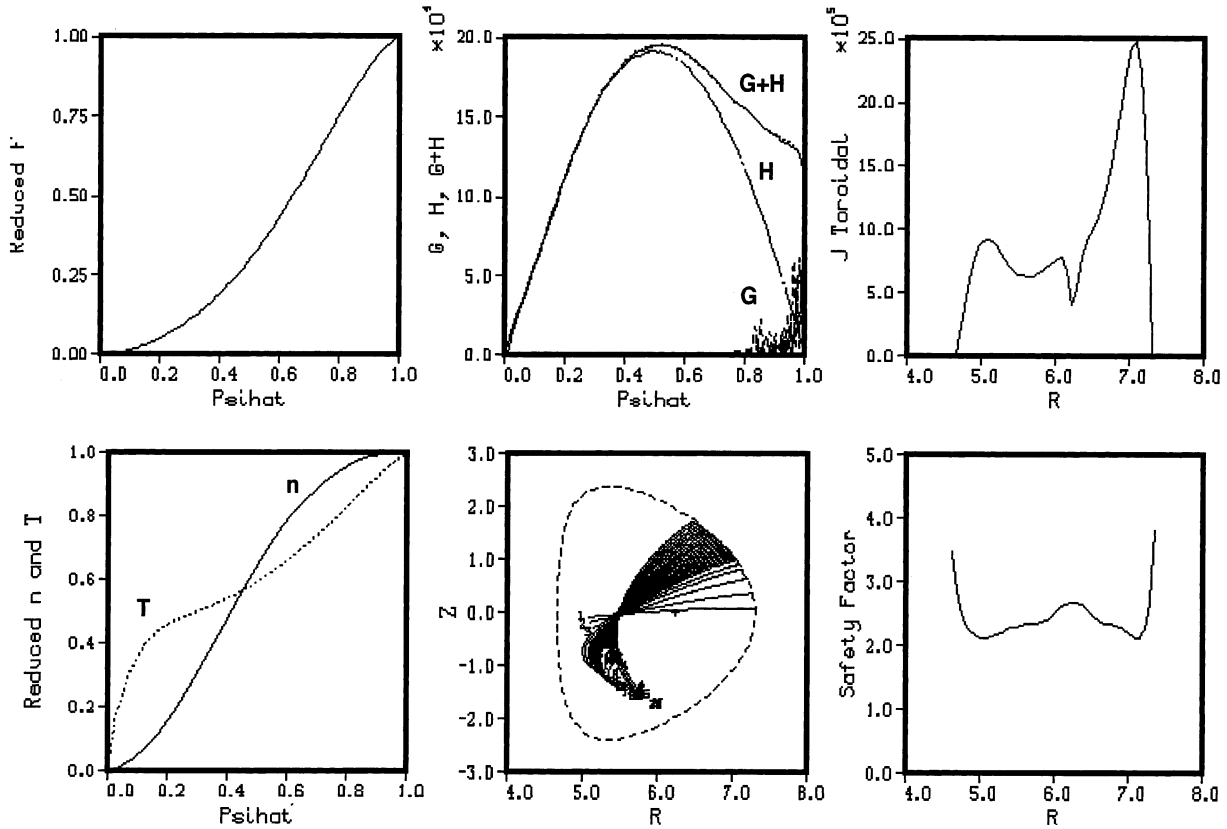

Fig. 5. Converged equilibrium from RIP fast-wave ray tracing calculations. Counter clockwise from top left: (1) Plasma diagmatism function; (2) Bootstrap (dash-dot), fast-wave driven (dash) and total driven (solid) current density profiles; (3) Toroidal current density; (4) Normalized density (solid) and temperature (dotted) profiles; (5) Fast-wave ray trajectories; (6) Safety factor. Note: Psihat $\equiv 1-\hat{\psi}$, and R is the major radius.

plasma. This result is for on-axis plasma parameters of $T_{e0}=22$ keV, $T_{i0}=20$ keV and $n_{e0}=2.9\times10^{20}$ m^{-3}, with $\bar{T}_e=14$ keV and $\bar{n}_e=1.7\times10^{20}$ m^{-3}. The converged equilibrium has $\beta_N=4.3\%$, $\beta=4.6\%$, $I_p=10$ MA, $q_*=2.2$, $q_0=2.6$, $q_{min}=2.1$ and $\ell_i(3)=0.45$, corresponding closely to the initial target.

Because of the broad, high T_e profile and low edge density, this plasma is nearly collisionless, with $\nu_{*e}<0.1$ over most of the plasma volume. At an aspect ratio of 4.5, electron trapping is modest (the trapped to circulating ratio if 1.08 at the edge) and the neoclassical reduction in the Ehst–Karney CD efficiency scaling [29] is moderate for FWCD near the axis, with the efficiency typically about 80% of that in the absence of trapping. The total CD power in this case is found to be $P_{FW}=59.2$ MW, giving rise to a bootstrap-aided CD efficiency $\gamma_B=1.73\times10^{20}$ A W^{-1} m^{-2}. At 78 MHz, the wall-plug-to-RF power conversion efficiency if $\eta_{cd}=0.80$.

Additional ICRF-driven RS equilibria were calculated with RIP in a reactor-relevant range of $\bar{T}_e$ values. In all cases the broad temperature profile results in nearly collisionless, banana regime operation. The best empirical fit to the CD efficiency scaling with temperature, at $A=4.5$, is given by $\gamma_B=0.38\bar{T}_e^{0.56}$, where $\bar{T}_e$ is in keV.

3.4. Current-drive efficiency scalings

3.4.1. Dependence on Z_{eff}

In the ARIES-RE design studies, the concept of a radiative mantle just inside the separatrix to radiate a substantial portion of the plasma heat flux was investigated. Since this idea involves the injection of high-to-medium Z impurities into the plasma (thus raising $Z_{\rm eff}$) and operation at a high edge density ($n_{\rm ea}/n_{\rm e0} \sim 0.2$), their implications for bootstrap current alignment and current-drive efficiency become an issue. In order to examine them, the optimum fit approach has been used to obtain scalings of $\gamma_{\rm B}$ with respect to $Z_{\rm eff}$ and volume-averaged temperature, $\bar{T}_{\rm e}$, for a strawman reversed shear equilibrium, with $A = 4.0$, $\beta = 4.92\%$ and $I_{\rm p} = 10$ MA. The following profiles have been assumed: $p/p_0 = (1 - \hat{\psi}^{1.3})^2$, $n_{\rm e}/n_{\rm e0} = 0.8(1 - \hat{\psi}^{\alpha_n})^{\beta_n} + 0.2$ and $T_{\rm e}/T_{\rm e0} = (p/p_0)/(n_{\rm e}/n_{\rm e0})$ and the profile factors, $\alpha_{\rm n}$ and $\beta_{\rm n}$, are adjusted to minimize the core bootstrap overdrive.

A series of current drive calculations were carried out for three values of $Z_{\rm eff}$ (1.5, 2.0, 2.5) at $\bar{T}_{\rm e} = 8$, 12, 16 and 20 keV. Again, vanadium impurity is introduced with a constant 14% concentration of helium ash. The results are given in Fig. 6. In this figure, the dashed curves are obtained directly from current drive calculations with an optimum match. To take into account errors that may occur in the matching process, the points corresponding to each value of $Z_{\rm eff}$ are fitted with a smooth dash-dotted curve of the form $\gamma_{\rm B} = \alpha_{\rm B}\bar{T}_{\rm e}^{\beta_{\rm B}}$, as discussed in a following subsection. For comparison, a typical $\gamma_{\rm B}$ scaling with respect to $\bar{T}_{\rm e}$ at $Z_{\rm eff} = 1.69$, but with $n_{\rm ea} \approx n_{\rm e0} \approx 0$, is also shown as a solid line in the same figure. These fitted curves are subsequently used in the power plant systems analysis.

For a fixed value of $Z_{\rm eff}$, $\gamma_{\rm B}$ increases with $\bar{T}_{\rm e}$, as predicted by theory. There are two effects that need to be accounted for. At a fixed β value, higher $\bar{T}_{\rm e}$ means lower $\bar{n}_{\rm e}$ and generally leads to a less collisional plasma and higher CD efficiency. At lower $\bar{T}_{\rm e}$, the density profile needs to be flattened to minimize or eliminate bootstrap current overdrive in the core. Around $\bar{T}_{\rm e} \approx 8$–12 keV and at higher values of $Z_{\rm eff}$, it is not always possible to eliminate the bootstrap overdrive, resulting in substantially lower $\gamma_{\rm B}$, since additional power is now needed to offset the overdrive.

From Fig. 6, it is observed that the value of $\gamma_{\rm B}$ decreases with $Z_{\rm eff}$. This result is not surprising because a high $Z_{\rm eff}$ can lead to three effects:

- A plasma with higher collisionality which implies lower CD efficiency;
- lower bootstrap current, particularly near the plasma edge where current drive is inefficient because of the relatively high density ($n_{\rm ea}/n_{\rm e0} = 0.2$) and low temperature; and
- enhanced ICRF fast wave absorption by impurity cyclotron resonances, although this effect is usually small.

The results of this parametric study indicate that the injection of impurities into the plasma severely degrades the overall current-drive efficiency. The fast that there is a substantial edge density, as required by an ELMy H-mode operation outside the RS region, also implies that a larger fraction of the CD power will be in the

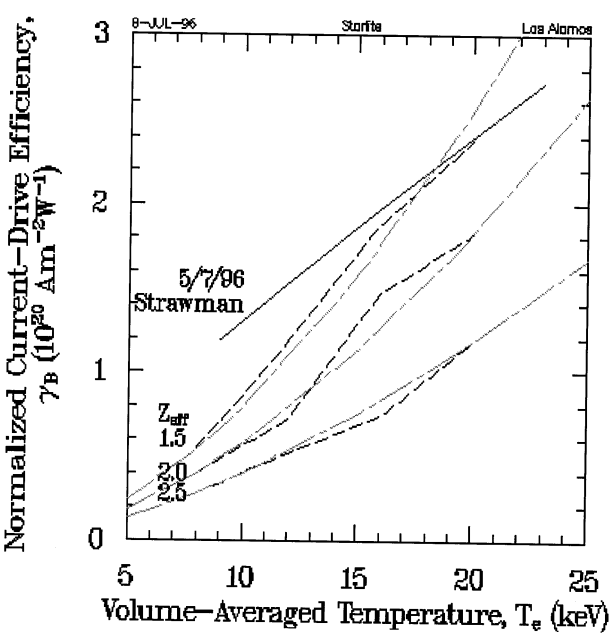

Fig. 6. Bootstrap-aided normalized current-drive efficiency scalings with plasma temperature for three values of $Z_{\rm eff}$, calculated using the reference reversed shear equilibrium. Smooth empirical fits to calculated scalings are used for systems analysis. A typical efficiency scaling with $Z_{\rm eff} = 1.69$ and zero edge density is shown for comparison.

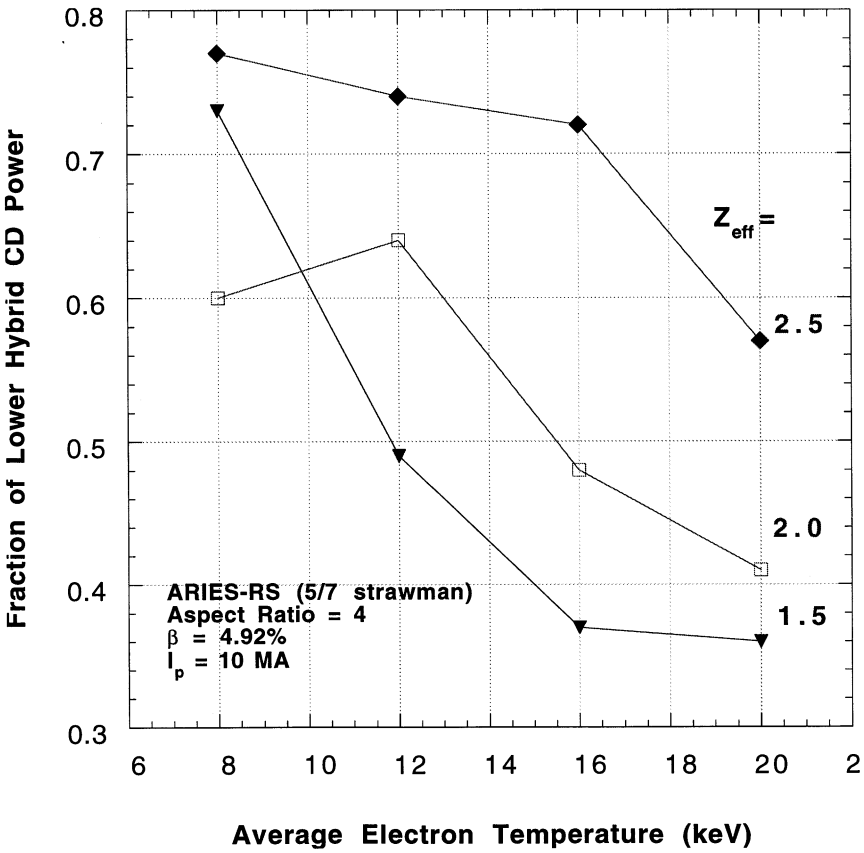

Fig. 7. Scaling of lower-hybrid current-drive power fraction with volume-averaged electron temperature and Z_{eff}.

lower hybrid system, which has the highest unit power cost among the three RF systems. The required LH current-drive power fraction is plotted as a function of $\bar{T}_e$ for $Z_{\text{eff}} = 1.5$, 2.0 and 2.5 in Fig. 7. It is clear that the LH power fraction increases at higher Z_{eff} and lower temperatures.

3.4.2. Dependence on aspect ratio

The scaling of CD efficiency with machine aspect ratio has also been investigated in order to determine its optimum value in terms of economics and configurational attractiveness. MHD analysis indicates that lower A leads to high plasma β, but the issue of overall CD efficiency must be addressed.

A systematic study [30] using the optimum fit approach and the CURRAY ray tracing code indicates that the γ_B scaling with $\bar{T}_e$ is relatively insensitive to A for $3.5 \leq A \leq 4.5$. However, at $A = 3.0$, there is a substantial reduction in the γ_B value over the range of $\bar{T}_e$ of interest to power plants. It is noted that in this study, only the ICRF fast wave and HFFW systems have been used to match the seed current profiles and the results are expected to be slightly optimistic.

The RIP code has also been used to investigate the γ_B dependence on A. Using this code, reversed shear equilibria at $A = 4.5$, 4.0 and 3.0 have been examined. The stability and CD criteria used are not uniform among cases within this set of calculations. The target equilibria at $A = 4.5$ and 3.0 provided by JSOLVER are at the maximum (full) β found stable with a conducting wall located at $r/a = 1.30$, whereas the $A = 4.0$ case corresponds more closely to the conservative reference choice, i.e. β is 90% of the maximum and wall position at

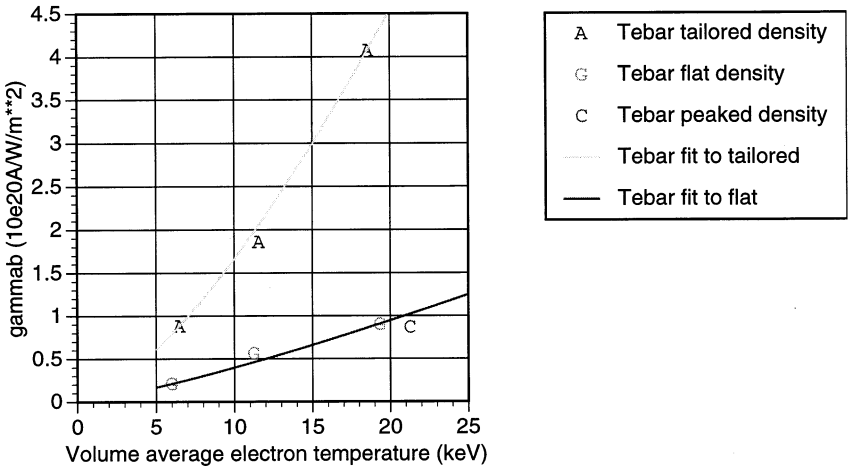

Fig. 8. Current drive figure of merit, γ_B, for both flat and peaked density profiles ($n_{e0}/\bar{n}_e = 1.17, 1.55$), and for an optimized 'ideal' density profile. The equilibria are converged and two or three RF current-drive systems are used.

$r/a = 1.25$ are assumed. In the $A = 3.0$ case, the CD result is simply matched to the target seed current provided by JSOLVER. In the $A = 4.0$ case calculation, an iterative, numerically stable, self-consistent solution is obtained, which has not been tested for stability. The most rigorous treatment was achieved only for the $A = 4.5$ case, as outlined in the previous subsection. Even though the analysis is not uniform, a discernible trend can nevertheless be identified: γ_B is lower with smaller A.

This decrease of γ_B at smaller A can be attributed to the increased magnetic trapping which results in lower CD efficiency. This effect is particularly strong if the density profile does not achieve a good bootstrap match to the stable equilibrium; a poor match necessitates rather inefficient off-axis CD. For the RIP calculations, in each case with nearly ideally chosen density/bootstrap profiles, the γ_B results at $A = 4.0$ are ~ 0.76 as large as the $A = 4.5$ results and the $A = 3.0$ results are ~ 0.47 as large as the $A = 4.5$ results. These conclusions from the RIP analysis are not inconsistent with those from the earlier CURRAY analysis. These results were included in the systems analysis to determine the best aspect ratio.

3.5. Sensitivities of current drive calculations

It is essential to point out that the calculated current-drive efficiency (γ_B) depends on many assumptions, including plasma characteristics which cannot be easily controlled or predicted. Therefore, there are uncertainties associated with the calculated γ_B for the RS power plant. The bootstrap current density profile is calculated from the Hirshman–Sigmar model with explicit velocity integration to account for finite collisionality. The theory is estimated (D.J. Sigmar, MIT Plasma Fusion Center, private communication, 1996) to be accurate to within about 15%. The FWCD and lower hybrid CD (LHCD) calculations of the seed current use either the Ehst–Karney formulation [29] or the treatment by Chiu et al. [31] which both fits an analytic expression known to be accurate to within only 12% of the Fokker–Planck results.

The strongest effect on the calculated CD efficiency comes from the density profile $n(\hat{\psi})$. In some cases off-axis current drive can be significantly reduced by detailed adjustments to $n(\hat{\psi})$. To illustrate this point, $n(\hat{\psi})$ is manually adjusted to differ from the reference profile in Fig. 2, in order to minimize the off-axis mismatch between the bootstrap and the stable target current density

for the $A = 4.0$ RS equilibrium This tailored density function varied slightly with $\bar{T}_e$ for a fixed β and the resulting large γ_B is shown (diamonds) in Fig. 8 at three different temperatures. The peakedness of these optimal density profiles varies in the range $1.37 \leq n_{e0}/\bar{n}_e \leq 1.55$ for the temperature range shown and the bootstrap fraction varies from 0.83 to 0.90. The reference case for the ARIES-RS power plant obtains a bootstrap fraction of 0.90, however, it utilizes some finite off-axis current drive to provide some degree of control for the location and depth of the q-minimum. In order to demonstrate the effect of untailored density profiles, these self-consistent calculations were repeated for a rather flat density profile, typical of ELM-free H-mode, with $n_{e0}/\bar{n}_e = 1.17$ and the figure shows (boxes) the resultant modest γ_B values at three different temperatures. Also shown is the calculated γ_B (triangle) for an arbitrary peaked density profile at $\bar{T}_e = 21$ keV, which likewise has a modest current drive efficiency. The flat and peaked density profiles are given by the form:

$$n(\psi) = n_0(1 - \psi^{b_n})^{a_n} \tag{5}$$

where $b_n = 1.4$ and $a_n = 0.25$ for the flat profile and $b_n = 2.75$ and $a_n = 2.4$ for the peaked profile. These non-tailored results typically display f_{BS} values ranging from 0.73 to 0.81. As is evident in the figure, the density profile can significantly affect the γ_B result, with optimally tailored profiles having CD efficiencies five times larger than for arbitrary profiles.

Thus, depending on the assumptions used in the calculations, the calculated γ_B value can vary considerably. In order to simplify the systems code calculations and to avoid an unwarranted appearance of accuracy, a simple analytic γ_B scaling, obtained from fitting a number of data points generated by calculations using the optimum fit approach, has been used. This analytic scaling has the form of $\gamma_B = \alpha_B \bar{T}^{\beta_B}$ for each pair of (A, Z_{eff}) values, as shown in Fig. 6. Considering the uncertainties related to the off-axis current-drive technique and the detailed density profile, it is misleading to assign more details to this formula.

A series of benchmarking calculations have been performed to check if the CURRAY and RIP codes generate similar current drives results. Since results from these codes quoted in this section are based on different profile assumptions, the comparison study was done using a simple equilibrium case generated by the RIP code, using three RF current drive systems and assuming the absence of energetic alphas. It is found that the ICRF fast wave and lower hybrid wave results agree well between the two codes, in terms of the power, $N_\parallel$ and launcher location requirements. In the case of HFFW, the power deposition profiles from the two codes differ in terms of the location and profile peakedness, using the same wave launch parameters. The resolution of this difference in the code results is a subject of future work.

4. Divertor physics

The high performance features of ARIES-RS, such as compactness and high power (> 500 MW), could lead to very high heat fluxes on its divertor structures. Material surfaces under such high heat loads are subject to severe thermal-related structural damage. Thus, to avoid compromising the structural integrity of the divertor it is necessary to reduce the heat fluxes to more manageable levels.

To avoid overheating the wetted divertor surfaces, the power flow into the scrape-off can be dispersed over a wider area of the vacuum vessel. One way this can be done is by enhancing the radiated power from the divertor and main plasmas, often referred to as 'radiating divertor' and 'radiating mantle' methods, respectively. In the former, excessive power flowing into the divertors is dissipated largely by radiating it away to adjacent divertor surfaces. In the latter, this power flow is radiatively dissipated at the edge of the plasma before it passes into the scrape-off layer (SOL). While both methods had their attractive features, the reference design settled on the 'radiating divertor' approach, since it was more consistent with the ARIES-RS physics constraints.

The radiated power generated in the cooler outer regions of the plasma (mantle) was examined with several recycling impurities assumed; neon, argon, krypton and xenon. Subject to the

requirements that $Z_{eff} < 2.3$ and the edge density and temperature coincide with those optimized for current drive and bootstrap current, no acceptable impurity would generate the necessary radiated power. Sufficient power could be radiated if the electron density near the plasma edge was high, the electron temperature there was lower and some level of enrichment in the divertor was achieved. Systems analysis indicates that although sufficient powers could be radiated with these assumptions, the consequences of increased current drive power, longer energy and particle confinement time, fuel dilution and decreased plasma power density made this unacceptable.

Thus, in this section we focus on efforts to produce a 'radiating divertor' solution to the Starlite divertor heat flux problem. To estimate the radiating capability of the scrape-off and divertor plasmas, we modelled the divertor and upstream electron density and temperature distributions using an analytic two point approximation, augmented by experimental results from double-null radiative divertor experiments on DIII-D.

4.1. Divertor physics modelling

We model the SOL and divertor plasmas based on the methodology developed by Barr and Logan [32]. In our analysis the assumptions are:

1. There is electron pressure balance along the scrape-off and divertor magnetic field lines.
2. Electron and ion temperature are equal.
3. Energy transport parallel to the magnetic field is mainly due to electron thermal conduction.
4. The midplane power scrape-off width is 0.02 m.
5. Coronal equilibrium is assumed.
6. The ratio of the impurity ion density to electron density is constant, unless specified.
7. Heat flux on the outboard divertor leg is described by $q_{div} = \gamma_T n_{div} C_s T_{div}$, where C_s is the poloidal component of the flow velocity at the sheath, γ_T is the power transmission coefficient, n_{div} and T_{div} are the electron density and temperature at the divertor strike points.
8. Z_{eff} includes both helium and impurity species in the main plasma, with a helium fraction in the core of 14% of the total ion density.
9. Electron density at the midplane edge of the plasma is taken as input.

The SOL plasma was divided into four radial flux zones, where each zone connected a midplane scrape-off location to the corresponding divertor location. Characteristic electron temperature, density and emissivity distributions were determined for each zone. Specifying the particle heat flux profile on the divertor structure and the electron density profile at the midplane, the electron temperature and density profiles at the divertor strike points and electron temperature profile at the midplane were determined. Once the electron density and temperature distributions along each particular zone is determined, then the radiated power along the zone is calculated.

In order to dissipate the heat flux, a set amount of power must be radiated along these zones in the divertor. The ratio of impurity density to electron density in the divertor region is adjusted to obtain this radiated power level. The enhancement of radiation in the divertor using impurities that are assumed not to affect the core plasma is called 'enrichment'. The processes producing enrichment are quite complex and still an active area of research and therefore in this study the enrichment will be specified without further justification.

4.2. Radiating divertor

The most difficult power handling problem involves the outer divertor since 80% of the power flows to the outboard side of the plasma. The power loading on the inboard divertor structures is much lower and experimental data indicates that the power is efficiently radiated over the entire length from the x-point to the divertor strike point. On the other hand, the outboard divertor is expected to have significant particle loading in addition to the radiation. Therefore, the analysis will focus on methods for dispersing the power flowing into the outboard scrape-off plasma. Two methods were examined, the radiating mantle and the radiative divertor.

For the radiative divertor case, the impurity chosen was neon, since this atom radiates efficiently in the cooler scrape-off and divertor regions. While the higher Z impurities can also

radiate efficiently their impact on the core plasma is more severe than the lower Z neon. These studies indicated that adding neon to the plasma system, under conditions consistent with other analyses (i.e. MHD stability, current drive, bootstrap current and transport), would radiate a sufficient amount of power in the SOL and divertor regions to make a feasible divertor solution.

For the reference plasma conditions described by; $P_{SOL} = 426$ MW, $n_e(a) = 0.62 \times 10^{20}$ m^{-3}, $n_e(a)/n_e(0) = 0.2$, a solution is found with $n_{neon}/n_e = 0.008$, $Z_{eff} = 2.0$, a midplane power scrape-off length of 0.02 m and flux expansion at the divertor strike point of three. In this case, the sum of particle and radiation heat flux does not exceed 6 MW m^{-2}. The enrichment factor to obtain the necessary radiated power in the divertor was in the range of two to eight. Although this is high for present day tokamak experiments, is not considered unrealistic. Considering only the divertor physics, reductions in this enrichment factor can be obtained by radiating more power from the plasma core and raising the plasma edge density. However, these adversely affect the current drive, MHD stability and plasma power balance.

In conclusion, a radiative divertor solution was utilized to dissipate enough of the transport power exiting the plasma to make heat loads on the divertor tolerable. This was done by injecting impurities with good radiating properties at divertor-like temperatures. Neon was chosen based on it having the least impact on the density, temperature and current density of the main plasma for ARIES-RS. Although a solution has been found, further optimization among the various constraints of MHD stability, current drive, divertor physics and overall systems is expected to produce improved solutions. The particle heat flux distribution for the outboard divertor is shown in Fig. 9, as a function of radial location projected back to the midplane SOL. The distribution of the radiated power within the 0.02 m scrape-off zone is also shown in Fig. 9 between the x-point and divertor surface. Radiated power peaks near the divertor surfaces while the particle heat flux peaks just below this position. This region is where the total heating would be at the highest.

5. Plasma operating regime and startup

5.1. POPCON analysis

A Plasma OPerating CONtour (POPCON) plot provides a rudimentary indication of a startup trajectory and thermal stability of the steady-state operating point. To generate the contours of the auxillary power required for steady-state plasma power balance as a function of fuel density and temperature with the McPOP code [33], the following assumptions are made: ITER-89P confinement scaling [34] with a multiplier, $H = 2.339$; plasma current, $I_p = 11.32$ MA; $I_p/a_pB_T = 1.028$

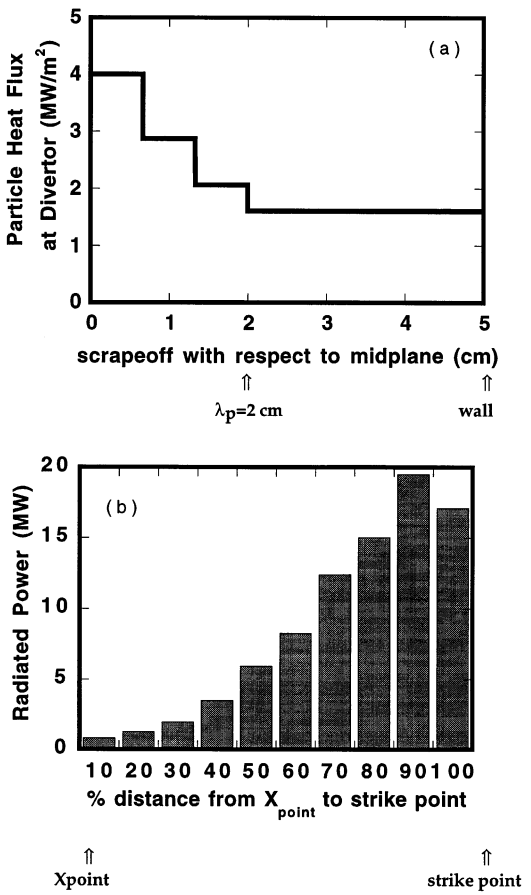

Fig. 9. The particle heat flux distribution for the outboard divertor as a function of radial location projected back to the midplane SOL (a), and the distribution of the radiated power within the 0.02 m SOL between the x-point and the divertor (b).

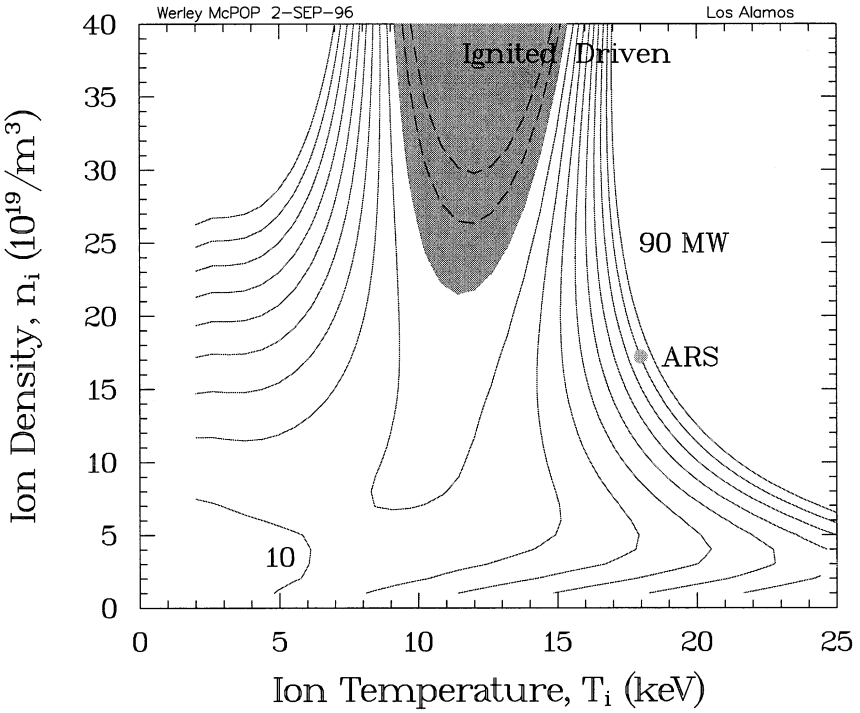

Fig. 10. Plasma operating contours of the auxillary power (in increments of 10 MW) required for steady-state plasma power balance displayed in ion density and temperature space for the following assumptions: ITER-89P confinement scaling [34] with a multiplier $H = 2.339$, $I_p = 11.32$ MA, $I_p/a_pB_T = 1.028$ MA mT^{-1}, $a_p = 1.38$ m, $f_{Ne} = 0.0055$ and $\tau_p^*/\tau_E = 10$.

MA mT^{-1}; plasma minor radius, $a_p = 1.38$ m; Neon concentration, $f_{Ne} = 0.0055$; and a ratio of particle-to-energy confinement times, $\tau_p^*/\tau_E = 10$. The energy and particle confinement times are discussed in Section 5.3. The resulting contours of auxillary power are displayed in Fig. 10. Ignited plasmas are possible for fuel temperatures in the range of $9 \leq T_i \leq 15$ keV and fuel density $n_i > 2 \times 10^{20}$ m^{-3}. In regions outside of the ignition region in Fig. 10, transport and radiation losses exceed the fusion power and auxillary power is required for steady-state operation. The ARIES-RS operating point is maintained with an auxillary power of 80.8 MW.

Thermal stability may be summarised from Fig. 10. An increase in temperature at constant density is seen from Fig. 10 to require additional auxillary power to maintain steady state. Similarly, an increase in density at constant temperature requires additional auxillary power to maintain steady state. Detailed thermal stability analysis would be required to include the complex interdependence of the transport, radiation, MHD stability and auxiliary power.

5.2. Plasma startup

The plasma startup is carried out in three phases. In the first phase, the plasma current is ramped up to 6 MA inductively in about 40 s. Here, it is imperative to ramp the plasma current up fast enough to keep the current profile broad. The plasma is grown off an outside limiter from a large circular plasma to full size and shape during this time, with slight heating being applied in the rampup to aid in maintaining a broad current profile.

In the second phase, the plasma current remains at 6 MA for about 200 additional seconds as strong heating is applied to increase the plasma pressure to $\beta_N \approx 2$. Current drive is applied to increase the off-axis current to about 2 MA, while

the bootstrap current increases to about 4 MA. During this period, the plasma current profile becomes hollow, making the internal inductance low. At the end of this period, the q-profile has become reversed shear.

In the final phase, plasma pressure is increased to the full flat-top value and the plasma current is increased to 11.3 MA, of which 10 MA are supplied by the bootstrap current. A transition to a peaked density gradient inside the region with zero magnetic shear takes place during this second heating phase, as is experimentally observed.

The startup trajectory to flat-top that requires the minimum auxillary power follows the valley floor (in auxillary power) between a radiation (i.e. bremsstrahlung and line radiation) hill at low temperature and a transport hill at high temperature that results from increasing power levels, decreasing confinement times and increasing ash concentration with increasing temperature. This optimal trajectory requires a maximum of ≈ 15 MW of auxillary power at $T_i \approx 7$ keV and $n_i \approx 6 \times 10^{19}$ m^{-3}. The startup trajectory to the ARIES-RS operating point requires four times more power than the optimal startup trajectory, but the maximum auxillary power occurs at the final operating point, because the operating point resides on the side of the high-temperature transport hill.

5.3. Energy and particle confinement

As was mentioned in the chapter introduction, plasma transport is not explicitly modelled. Plasma temperature and density profiles are only made to roughly agree with theoretical and experimental observations for reversed shear configurations. The global plasma energy confinement time is determined by the systems code to provide plasma power balance. The energy confinement time is 1.34 s, which corresponds to an ITER-89P scaling multiplier of 2.34. This value is within the present experimental bounds for reverse shear plasmas, as well as other plasma operating modes.

The particle confinement time in the main plasma is expected to track the energy confinement time. Thus, any increase in the energy confinement time results in a corresponding increase in the particle confinement time. The primary issues arising from the particle transport are the removal of helium ash and fueling requirements for deuterium and tritium. The confinement time for particles in the plasma chamber (referred to as the effective particle confinement time, τ_p^*) is considerably longer than the confinement time in the main plasma, due to recycling and the limited particle removal by pumping. However, a particle is known to re-enter the main plasma many times during its stay in the plasma chamber. Experiments [36,37] on helium removal which used significant active pumping, indicate that the ratio τ_p^*/τ_E is in the range 7–15. It is difficult to accurately determine the corresponding particle confinement time in the main plasma due to the complexity of recycling, but estimates are in the range $\tau_p/\tau_E \approx 1$–2. For the ARIES-RS design τ_p is equal to τ_E and $\tau_p^*/\tau_E = 10$.

5.4. Edge conditions and ELMs

Diverted plasmas invariably transition to the H-mode above a certain threshold transport power, P_{thr}, crossing the confined plasma into the SOL. Numerous scaling studies [42–45] have resulted in semi-empirical formuli for this L to H transition:

$$P_{thr} = 0.04\bar{n}SB \tag{6}$$

$$P_{thr} = 0.025\bar{n}^{0.75}SB \tag{7}$$

$$P_{thr} = 0.169\bar{n}S^{0.7}B \tag{8}$$

$$P_{thr} = 0.3\bar{n}R^{2.5}B \tag{9}$$

Here P_{thr} is in MW, $\bar{n}$ is the line average electron density (10^{20} m^{-3}), S is the plasma surface area, R the major radius, B is the on-axis vacuum toroidal field (T) and dimensions are in meters. Referring to the POPCON plot, a preferred low density startup path would have $n = 0.3$ (high enough to avoid locked modes) and a full bore plasma would achieve the L to H transition at $P_{thr} = 36$, 30, 25, or 46 MW, for the four respective scalings. Other scalings have also been proposed, but the four scalings reproduced here show the typical range of predicted P_{thr}. The power flow into the SOL is $P_{tran} = P_\alpha + P_{aux} - P_{rad}$ and

for startup, $P_{tran} \approx P_{aux} = 80$ MW. So the auxiliary heating power is expected to be more than sufficient to force the plasma into a H-mode at low densities.

At full power operation $\bar{n} = 2.5$, so larger P_{tran} is needed for H-mode, however the H-mode is robust, showing a hysteresis such that the reverse H to L transition is maintained with coefficients about half those in the formuli above. At the reference operating point the four formuli would require, respectively $P_{thr} = 150$, 110, 105, or 190 MW to remain in the H-mode. Steady state power balance for our machine has $P_{tran} = P_{\alpha} + P_{aux} - P_{rad} = 400$ MW, therefore, the plasma is expected to remain in the H-mode.

If P_{tran} were just above the threshold for H-mode operation, then the edge pressure gradient would fluctuate via Type III edge localized modes (ELMs) at values around 30–50% of the first regime ballooning limit. At higher P_{tran}, the Type III ELM frequency (f_{ELM}) decreases and with adequate P_{tran}, the ELMs vanish and ELM-free (EF) operation is possible. In experiments, the EF mode is frequently undesirable as the density rises uncontrollably, due to excellent particle confinement near the edge. This would likewise cause difficulties for a power plant, as high helium ash concentrations would result. Fortunately, for plasmas with P_{tran} greatly exceeding the H-mode threshold value, ELMs reappear. At first Type I, or 'giant', ELMs appear, which are potentially devastating to plasma facing components (PFC). With increasing P_{tran} these ELMs continuously degrade into low amplitude, high frequency Type II, or 'grassy' ELMs, as the edge pressure gradient is pushed into the second ballooning stability region. Grassy ELMs are highly desireable for practical operation, as the H factor is nearly as good as the EF operation, but particle confinement is low enough to exhaust and recycle helium near the plasma edge. We surveyed several tokamaks (DIII-D, ASDEX U, TFTR, JT-60) and found the following approximate correlation for Type I and II:

$$f_{ELM} = C_E Q_{sep} \bar{n} / I_p \tag{10}$$

where $Q_{sep} = P_{tran}/S$ (MW m^{-2}), I_p is the toroidal plasma current (MA), f_{ELM} is given in Hz and $C_E = 1600$–8900, for all cases with $f_{ELM} > 70$ Hz. Our design, with $Q_{sep} = 0.8$ MW m^{-2} should operate with grassy ELMs at $f_{ELM} = 300$–1700 Hz.

Controlling the edge plasma density (n_{edge}) at the (separatrix) boundary is important for avoiding disruptions. The Borrass theory depends on impurity content and has been semi-empirically fit for two large tokamaks [33–40] (P.B. Parks, General atomics, private communication, 1996) [41];

$$n_{edge} < 0.5 Q_{sep}^{0.57} B^{0.31} / (q_* R)^{0.09} \tag{11}$$

$$n_{edge} < 1.23 Q_{sep}^{0.66} B^{0.33} / (q_* R)^{0.06} \tag{12}$$

The former formula applies to carbon tiles on ASDEX and the latter to beryllium on JET (a lower Z_{eff}). Here, n_{edge} is 10^{20} m^{-3} and q_* is the effective safety factor. For our device with $Q_{sep} = 0.8$ MW m^{-2}, these limits are, respectively, $n_{edge} < 0.64$ and 1.75. Considering the high impurity level of our design ($Z_{eff} = 1.7$) prudence dictates an edge density $n_{edge} < 0.6$ in order to avoid disruptions.

An additional edge condition is correlated with ELMing H-mode, namely a minimum electron temperature, T_{edge}, at the separatrix (boundary). On TFTR [44] this required on the 95% flux surface. These edge temperatures are evidently associated with the high heating power which pushes the edge plasma near the first ballooning regime limit.

5.5. Radiation from the main plasma

A high-temperature magnetized plasma will radiate cyclotron, line radiation and bremsstrahlung, the levels depending on the distribution of plasma density, temperature and the species present. It is generally desirable to have some fraction of the total plasma power radiated, since this reduces the power that goes to the divertor in the form of energetic particles. In addition the radiation is emitted isotropically, helping to deposit the power over a large area (the first wall surface). Typically the cyclotron radiation lost is small for conventional tokamak parameters, due to a highly reflective first wall.

Bremsstrahlung is predominantly emitted from the plasma core and line radiation from the cooler boundary region. It has been proposed that line radiation from the cooler boundary could be enhanced with higher Z species while having a minimum impact on the plasma core performance [38]. However, enhancing the radiation can have several side-effects. It is understood that the higher Z impurity will penetrate to the core of the plasma and contribute to greater bremsstrahlung radiation in addition to the increased line radiation. The increased radiation loss from the plasma will lead to longer energy confinement times to maintain plasma power balance, which consequently increases particle confinement times and helium dilution. The introduction of the high Z impurity must also increase Z_{eff}, which reduces the current drive efficiency in the plasma, thereby requiring higher powers to drive the same current. Finally, increasing the radiation in the plasma edge region, which requires that the density be increased there, leads to reduced bootstrap current. If this current must then be supplied by external current drive, it leads to significant increases in the overall current drive power and ultimately the recirculating power for the reactor.

In order to study this tradeoff quantitatively, equilibria were generated with varying plasma density profiles reflecting increasing finite edge density, along with the resulting bootstrap current profile. Examples of these equilibria are shown in Fig. 11, giving the total plasma density, temperature and parallel current density profiles. These should be compared with those in Figs. 1 and 2 for the reference configuration. The bootstrap current fraction and required current drive change to 0.86 and 1.36 MA for $n(a)/n_0 = 0.2$ and to 0.83 and 1.66 MA for $n(a)/n_0 = 0.4$. Both configurations are ideally MHD stable and it is important to point out that for these edge densities one does not have to drive the lost bootstrap current at the plasma edge to maintain stability. This region would have very low current drive efficiency and fortunately can be neglected. In addition, the coronal equilibrium radiation model [33] was included in the equilibrium calculation to provide the detailed radiation profile. From these calculations it was found that although the radiation could clearly be enhanced by introducing impurities (argon, xenon and krypton were examined), it was predominantly from the core plasma (not the cooler boundary region) unless the plasma edge density was greater than 40% of the peak value.

Current drive calculations were carried out with these equilibria to determine the impact on current drive efficiency of the reduced bootstrap current and higher Z_{eff}. This data was then included in the system code (which evaluates the plasma power balance with all radiation contributions present) in order to determine the tradeoff between enhanced radiation and the overall device performance.

The systems analysis showed that efforts to enhance radiation, which was to reduce the transport power to the divertor, produced no reduction or actually increased the transport power. The reason for this was primarily from increased current drive power, necessary to compensate for impurity and density profile effects. In addition, the increased current drive power and enhanced radiation led to increased energy confinement time, fuel dilution and lower power density. This nullified any benefits to enhancing radiation from the core or mantle regions of the plasma. Consequently, the Z_{eff} remains at 1.7 and the edge plasma density ratio is set at $n(a)/n_0 = 0.2$ for the reference plasma. However, enhancing the radiation from the SOL and divertor region was found to be acceptable and is discussed in Section 4.

5.6. Plasma fueling

In a fusion power plant, the D/T fuel ions in the plasma core are constantly lost through fusion reactions and pumping in the divertor channel. Therefore, the plasma core must be replenished with fuel ions in order to maintain power and particle balance. In the ARIES-RS design, high-speed pellet injection is considered as the reference plasma fueling scheme, because it has an impressive data base and is now routinely used in present-day tokamak experiments. However, the pellet injection speed required for deep fueling of the plasma core must be determined.

Substantial work has already been undertaken on the physics of pellet ablation inside a burning

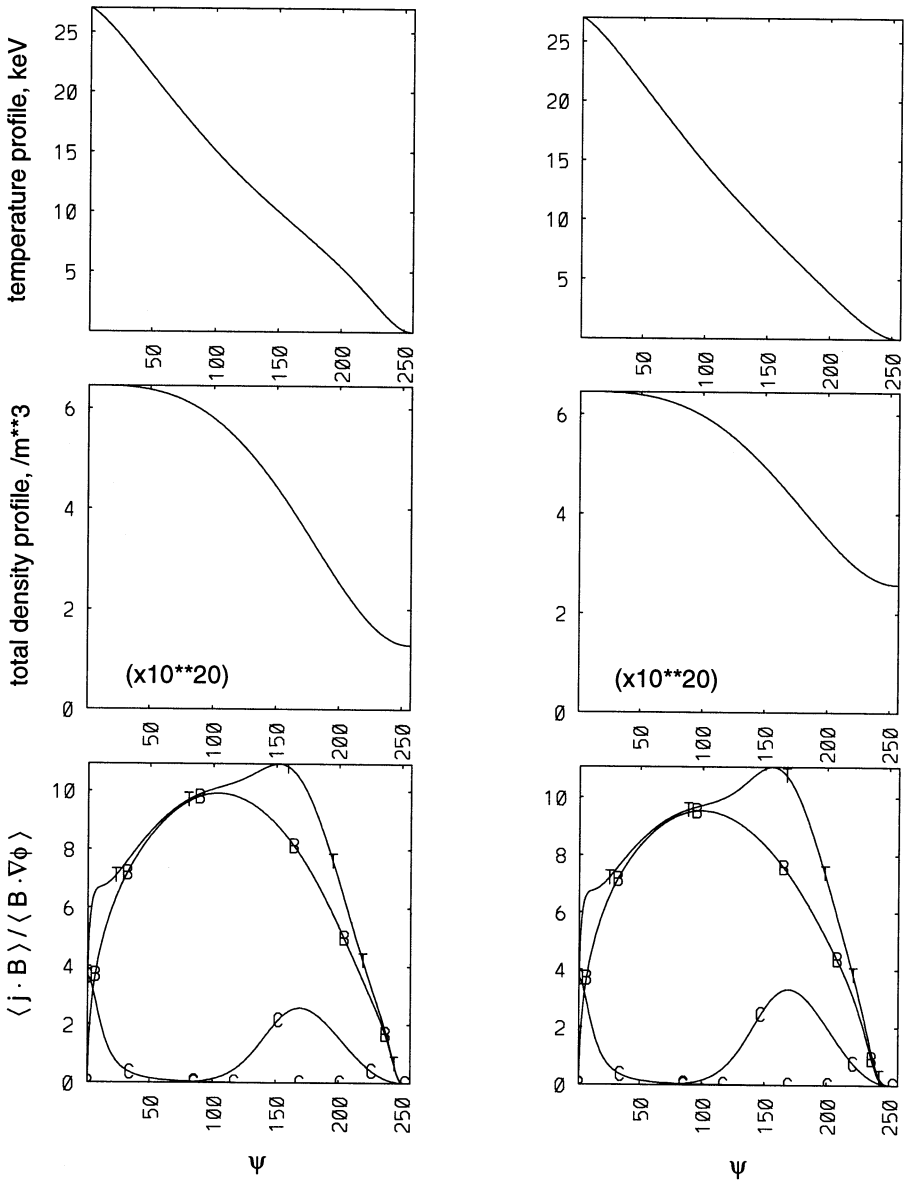

Fig. 11. The total plasma density, temperature, and parallel current density as a function of poloidal flux for the two cases with $n(a)/n_0 = 0.2$ and $n(a)/n_0 = 0.4$.

plasma. The theory and related literature were described in the ARIES-I design report [23] and will not be repeated here. In this subsection, the results of calculations aimed at determining the fueling requirements are presented.

Several constraints and criteria need to be satisfied for a pellet injection scheme used in a reversed shear plasma. First, it is postulated that, as long as the bulk of the injected pellet is ablated anywhere inside the minimum-q surface (where there is a transport barrier), the inward particle transport should carry the deposited fuel into the core region. In other words, it is considered sufficient to inject and deposit the fuel beyond the

minimum-q surface. Recent experimental results [39] on DIII-D and TFTR, where ion confinement inside the RS region was found to be better than neo-classical, appear to lend support to this assumption.

The optimum injection location is at the outboard equatorial plane and the trajectory should be along that plane in order to maximize the penetration depth. For the ARIES-RS plasma, the distance from the injection point to the magnetic axis is 0.928 m and that to the minimum-q surface is only 0.111 m, which corresponds to $\hat{\psi} = 0.71$ on the outboard side.

The second fueling criterion is related to the size of the pellet. In order to avoid quenching of the burn and to minimize the perturbations in the fusion power absorbed in the surrounding structures, the global density perturbation per pellet to the plasma, or the particle inventory fraction, should be less than 15%. Since the solid D/T molecular number density is fixed at 3.1×10^{28} m^{-3}, this criterion then limits the size of the pellet.

A plasma equilibrium similar to ARIES-RS has been used for the fueling calculations, with $\bar{n}_e = 2.57 \times 120$ m^{-3}, $n_{e0}/\bar{n}_e = 1.50$, $n_{ea}/n_{e0} = 0.2$, $\bar{T}_e = 13$ keV, $T_{e0}/\bar{T}_e = 1.84$ and $\tau_p^* = 11.3$ s. For deposition beyond the minimum-q surface, the required fueling rate is 6.0×10^{21} s^{-1}, of which 30% is due to fusion burnup and the rest due to pumping. Spherical pellets of four different sizes and injection (or repetition) rates have been examined and their parameters are listed in Table 6. Note that the particle inventory fractions for these pellets are all below the assumed 15% limit.

For the calculations, a simple but accurate pellet ablation model is used, in which the ablation rate is proportional to [40]

$$\frac{dr_p}{dt} \propto \frac{n_e^{0.33} T_e^{1.64}}{r_p^{0.67}} \tag{13}$$

Table 6
Pellet parameters for fueling calculations

Diameter (mm)	3	4	5	6
Inventory fraction (%)	1.8	4.3	8.4	14.5
Injection rate (Hz)	6.8	2.9	1.5	0.8

where n_e, T_e and r_p are the local electron density and temperature and pellet radius, respectively. The pellet is assumed to be a sphere composed of a 50–50 mixture of D/T solid.

The results of the calculations are summarized in Fig. 12, where the deposition fuel density per pellet is plotted along the equatorial plane for the selected pellet sizes and injection velocities. When the pellet penetration depth is defined to be the location from the outboard edge, where the particle ablation rate is highest is defined, it is clear from Fig. 12 that larger pellet size and higher injection velocity both lead to deeper penetration. On the other hand, at a fixed velocity, larger pellet size results in higher and broader local fuel deposition per pellet. At the same time, for a fixed pellet size, higher velocities give rise to reduced and broader local fuel deposition per pellet.

In the absence of one-dimensional plasma transport analysis, the maximum local density perturbation, $(\delta n/n)_{max}$, along the pellet trajectory is an important quantity to consider. This quantity should be minimized in order to ensure plasma profile stability and a steady fusion power output. In Fig. 13, $(\delta n/n)_{max}$ is plotted against pellet velocity for the four pellet sizes listed in Table 6.

For the ARIES-RS design point, a pellet diameter of 4 mm has been chosen, with a required injection speed of 5 km s^{-1} at a repetition rate of 2.9 Hz. At these parameters, the peak deposition occurs about 2 cm inside the minimum-q surface, the maximum local density perturbation per pellet is a reasonable 23% and the particle inventory fraction is 4.3%.

There are several issues that must be addressed. First, pellet ablation should not perturb the local pressure and its gradient since the pellet is 'cold'; thus, a robust equilibrium will not be destabilized as long as the perturbation is moderate. Local changes in the density profiles will not perturb the bootstrap current profile in a short time scale, as the skin time is long due to high local T_e. Secondly, the population of fast electrons due to LH current drive should be small because of low T_e and high n_e in its region of operation and thus should not significantly impact the pellet deposition profile. Even if it is significant, this effect can

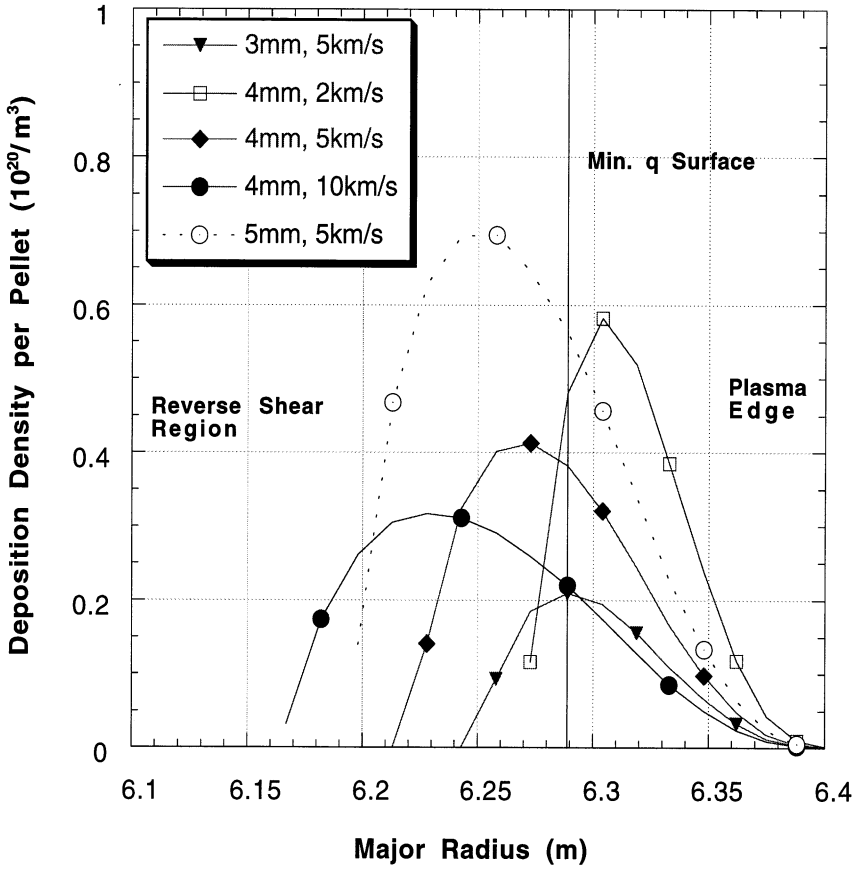

Fig. 12. Maximum local density perturbation per pellet along injection trajectory for various pellet velocities and sizes. Design point is also indicated.

be avoided by momentarily turning off the LH power during the very short time interval (~ 40 μs) when the pellet is fired, as has been demonstrated on Tore-Supra. Thirdly, the effect of pellet ablation due to energetic alphas is deemed to be small [40]. Nevertheless, in the region outside the minimum-q surface, the population of energetic alphas may be too small to make this effect significant. Finally, as discussed in detail below, giant ELMs have been observed to be triggered during pellet injection. In a power plant environment, methods will have to be found to suppress or avoid these activities in order to preserve the divertor tiles.

6. Disruptions and thermal power transients

Thermal transients arise from various tokamak events: major disruptions, vertical displacement events (VDE), minor disruptions, pellet fueling (200 MW m^{-2} observed on DIIID divertor tiles), giant ELMs (Type I), grassy ELMs (Type II), sawteeth (unlikely with current drive), fishbones (alpha losses), as well as other kinetic modes and loss of control. The most serious erosion damage to plasma facing components (PFC) is from VDEs and major disruptions. Three parameters strongly influence the erosion damage: the thermal energy density, the impact time period and

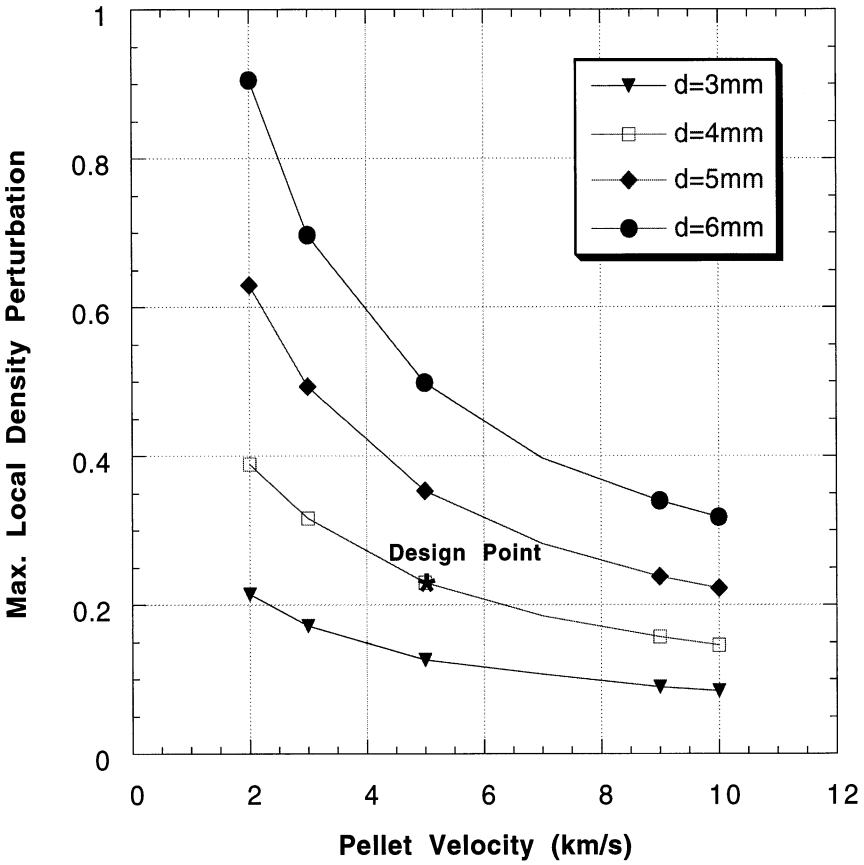

Fig. 13. DT fuel deposition profile per pellet along injection trajectory for various pellet sizes and injection velocities. For this RS strawman equilibrium, the magnetic axis is located at $R = 5.47$ m.

the kinetic energy of the plasma particles which impact the PFC. A survey of single-stage disruptions and VDEs (Compass D, TFTR, DIIID) shows that the plasma thermal decay lasts from 0.4 to 7.0 ms, although considerably shorter times have been observed on occasion. On JET Shot No. 11217 (3.7 MA) the major disruption had an almost 20 ms thermal dump. Thus τ_u is quite variable and we expect our design to be characterized by $\tau_u = 0.1-10.0$ ms as a typical range of values. The actual time behavior of the thermal dump is complicated in cases where it has been measured. Often there is evidence of multiple strikes within the period τ_u, as if the PFC is exposed to a rapidly rotating plasma footprint in the SOL. Calculations with DESIRE and A*THERMAL [46] suggest $\tau_u = 1.0$ ms yields the worst damage to a tungsten surface with energy density $U = 100$ MJ m^{-2} (assuming a simple sine wave thermal dump). Longer τ_u allows more heat conduction into the PFC depth (less melting), while very much shorter τ_u permits more effective vapor shielding of the surface. At $\tau_u = 6$ ms the codes predict melt layers up to 0.23 mm thick. At much lower $U = 2$ MJ m^{-2} similar damage is observed in steel discs exposed to 10 ms heat pulses from MPD arcjet tests [47].

The value of U varies greatly in tokamaks. The thermal footprint typically is as wide as the usual heat load on the divertor. Any toroidal rotation is so rapid that we consider the disruption heat load to be axisymmetric during the period τ_u. When less than the total plasma energy is lost (without current decay), the event is a minor disruption.

Typical minor disruptions on DIIID and TFTR lose 30–50% of the plasma thermal energy. Although the tokamak may recover from the minor disruption, very often the event is a precursor to a major disruption (leading to current loss). Documented runs on TFTR, JET, JT60 and DIIID show fractional energy losses over a continuous range, 10–95% of the stored thermal energy for a variety of disruptions. Our reference design has 488 MJ of stored thermal energy. The impact area is estimated for a vertical thermal dump as 4.8 m^2, where it is assumed that only half the available area is contacted. Thus, minor and major disruptions span the range 10 MJ $m^{-2} < 100$ MJ m^{-2} for the reference design. The DESIRE calculations for a 0.8 ms sine pulse on W indicates a melt layer of 0.48 mm at 100 MJ m^{-2}, decreasing monotonically to 0.20 mm at 10 MJ m^{-2}. Additionally, vaporized tungsten is produced over this range of U; vaporized PFC is probably irreversibly lost from the PFC at each event. Such calculations generally agree with plasma gun tests of PFC materials. For example [48], gun pulses of 0.4 ms on aluminum show crater depths of 0.2 mm at $U = 30$ MJ m^{-2}, decreasing at smaller U.

The particle kinetic energies, E_e and E_i, incident on the PFC have been observed on JET, TEXTOR, TFTR and DIIID, where E_e and E_i are generally about equal to the edge temperature prior to disruption. We expect $E_e = E_i =$ 0.2–2.0 keV in the reference plasma. Calculations with DESIRE show that $E_e = E_i =$ 1.0 keV result in damage one to two orders of magnitude more severe than at 10.0 keV.

Less severe erosion occurs from single giant ELMs (typically 10% of the thermal energy is lost), but such Type I ELMs may occur at multi-Hertz frequencies, which would quickly destroy the PFC. Our design is predicted to have grassy ELMs which typically lose less than 1% of the thermal energy per event. Such kilohertz ELMs bring U below the threshold (2 MJ m^{-2}) for melting and vaporization. However, sputtering associated with the high particle flux can also be devastating in this regime. Our calculations indicate carbon erosion at 0.01 μm per event at 1 MJ m^{-2} and test stands confirm loss rates of this magnitude. Clearly this is a crucial area for further study if tokamaks are to operate with high frequency, low amplitude ELMs. The plasma current decay associated with disruptions is discussed in [49], which should be consulted by the interested reader.

7. Summary

The physics basis for the ARIES-RS power plant design has been established based on theoretical calculations and the experimental database. Detailed analysis was carried out for plasma equilibria and ideal MHD stability, bootstrap current, non-inductive current drive, SOL and divertor physics, plasma vertical stability and position control and plasma power balance. Plasma transport was not explicitly modelled, however, temperature and density profiles were constrained to agree with observed experimental trends and the global energy confinement time was found to be within the experimental database when extrapolated to reactor parameters.

The resulting configuration provides significant advantages over previous plasma models (ARIES-I, ARIES-II/IV and PULSAR) by achieving a high β of 4.96%, a high plasma driven current fraction of 91%, low total current drive power ≤ 80 MW and a divertor solution with maximum heating at the divertor plate of ≤ 6 MW m^{-2}. The plasma triangularity was maximized, but limited by the divertor and inboard neutron shielding. The plasma elongation was limited by the need to locate the stabilizing structure in the reflector to shield gap and the vertical position control feedback control power. It was possible to use the vanadium blanket structure for the kink stabilization shell. The current drive schemes included ICRF, HFFW and LHCD to provide the maximum flexibility in current profile control. The divertor solution utilizes neon impurity to enhance the radiation from the SOL and divertor. In addition, it was assumed that the plasma would enter the H-mode and would sustain 'grassy' ELMs which would be sufficient for helium ash removal.

References

[1] C.E. Kessel, J. Manickam, G. Rewoldt, W. Tary, Improved plasma performance in tokamaks with negative magnetic shear, Phys. Rev. Lett. 72 (1994) 1212.

[2] A.D. Turnbull, T.S. Taylor, Y.R. Lin-Liu, H. St John, High beta and enhanced confinement in a second stable core VH-mode advanced tokamak, Phys. Rev. Lett. 74 (1995) 718.

[3] F.M. Levinton, M.C. Zarnstorff, S.H. Batha, M. Bell, R.E. Bell, R.V. Budny, C. Bush, Z. Chang, E. Fredrickson, A. Janos, J. Manickam, A. Ramsey, G.L. Schmidt, E. Synakowski, G. Taylor, Improved confinement with reversed magnetic shear in TFTR, Phys. Rev. Lett. 75 (1995) 4417.

[4] E.J. Strait, L.L. Lao, M.E. Mauel, B.W. Rice, T.S. Taylor, K.H. Burrell, M.S. Chu, E.A. Lazarus, T.H. Osborne, S.J. Thompson, A.D. Turnball, Enhanced confinement and stability in DIII-D discharges with reversed magnetic shear, Phys. Rev. Lett. 75 (1995) 4420.

[5] L.L. Lao, K.H. Burrell, T.S. Casper, V.S. Chan, M.S. Chu, C.B. Forest, R.J. Groebner, F.L. Hinton, Y. Kawano, E.A. Lazarus, Y.R. Lin-Liu, M.E. Mauel, W.H. Meyer, R.L. Miller, G.A. Navatil, T.H. Osborne, T.S. Taylor, W.M. Tang, A.D. Turnball, R.E. Waltz, and the DIII-D Team, Confinement and stability of DIII-D negative central shear discharges, Plasma Phys. Control. Fusion 38 (1996) 1439.

[6] E.A. Lazarus, L.L. Lao, T.H. Osborne, T.S. Taylor, A.D. Turnball, M.S. Chu, A.G. Kellman, E.J. Strait, J.R. Ferron, R.J. Groebner, W.W. Heidbrink, T. Carlstrom, F.J. Helton, C.L. Hsieh, S. Lippman, D. Schissel, R. Snider, D. Wroblweski, An optimization of beta in the DIII-D tokamak, Phys. Fluids B 3 (1991) 2221.

[7] M. Hugon, B.Ph. van Milligan, P. Smeulders, L.C. Appel, D.V. Bartlett, D. Boucher, A.W. Edwards, L.-G. Eriksson, C.W. Gowers, T.C. Hender, G. Huysmans, J.J. Jacquinot, P. Kupschus, L. Porte, P.H. Rebut, D.F.H. Start, F. Tibone, B.J.D. Tubbing, M.L. Watkins, W. Zwingmann, Shear reversal and MHD activity during pellet enhanced performance pulses in JET, Nuc. Fusion 32 (1992) 33.

[8] G.T. Hoang, C. Gil, E. Joffrin, D. Moreau, A. Becoulet, P. Bibet, J.P. Bizarro, R.V. Budny, J. Carrasco, J.P. Coulon, C. De Michelis, T. Dudok De Wit, P. Monier-Garbet, M. Goniche, R. Guirlet, T. Hutter, S.M. Kaye, J. Lasalle, L. Laurent, P. Lecoustey, X. Litaudon, M. Mattioli, Y. Peysson, A.-L. Pecquet, G. Rey, S.A. Sabbagh, B. Saoutic, G. Tonon, J.C. Vallet, Improved confinement in high l_i lower hybrid driven steady state plasmas in Tore Supra, Nuc. Fusion 34 (1994) 75.

[9] F.M. Levinton, R.J. Fonck, G.M. Gammel, R. Kaita, H.W. Kugel, E.T. Powell, D.W. Roberts, Magnetic field pitch-angle measurements in the PBX-M tokamak using the motional stark effect, Phys. Rev. Lett. 63 (1989) 2060.

[10] X. Litaudon, R. Arslanbekov, G.T. Hoang, E. Joffrin, F. Kazarian-Vibert, D. Moreau, Y. Peysson, P. Bibet, P. Froissard, M. Goniche, G. Rey, J. Ferron, K. Kupfer, Stationary magnetic shear reversal experiments in Tore Supra, Plasma Phys. Control. Fusion 38 (1996) 1603.

[11] S. Ide, T. Fujita, O. Naito, M. Seki, Sustainment and modification of reversed magnetic shear by LHCD on JT-60U, Plasma Phys. Control. Fusion. 38 (1996) 1645.

[12] C.E. Kessel, The bootstrap current in a tokamak, Nuc. Fusion 34 (1994) 1221.

[13] J.M. Greene, M.S. Chance, The second region of stability against ballooning modes, Nuc. Fusion 21 (1981) 453.

[14] M.J. Gerver, J. Kesner, J.J. Ramos, Access to the second stability region in a high-shear, low-aspect-ratio tokamak, Phys. Fluids 31 (1988) 2674.

[15] T.S. Taylor, E.J. Strait, L.L. Lao, M. Mauel, A.D. Turnbull, K.H. Burrell, M.S. Chu, J.R. Ferron, R.J. Groebner, R.J. Lattaye, B.W. Rice, R.T. Snider, S.J. Thompson, D. Wroblewski, D.J. Lightly, Wall stabilization of high beta plasmas in DIII-D, Phys. Plasmas 2 (1995) 2390.

[16] A. Bondeson, D.J. Ward, Stabilization of external modes in tokamaks by resistive walls and plasma rotation, Phys. Rev. Lett. 72 (1994) 2709.

[17] A.H. Boozer, Stabilization of resistive wall modes by slow plasma rotation, Phys. Plasmas 2 (1995) 4521.

[18] A. Bondeson, M. Persson, Stabilization by resistive walls and q-limit disruptions in tokamaks, Nuc. Fusion 28 (1988) 1887.

[19] K. Ida, K. Kawahata, K. Toi, T. Wateri, O. Kaneko, Y. Ogawa, H. Sanuki, K. Adati, R. Akiyama, A. Ando, R. Ando, Y. Hamada, S. Hidekuma, S. Hirokura, A. Karita, T. Kawamoto, Y. Kawasumi, M. Kojima, R. Kumazawa, T. Koruda, K. Masai, S. Morita, K. Narihara, K. Ohkubo, Y. Oka, S. Okajama, T. Ozaki, M. Sakamoto, M. Sasao, K. Sato, K.N. Sato, T. Seki, F. Shimpo, Y. Taniguchi, T. Tsuzuki, H. Yamada, Observation of toroidal plasma rotation driven by the electric field induced by ion loss, Nuc. Fusion 31 (1991) 943.

[20] L.-G. Eriksson, R. Giannella, T. Hellsten, E. Kallne, G. Sundstrom, Observations of toroidal rotation induced by ICRH in JET, Plasma Phys. Control. Fusion. 34 (1992) 863.

[21] H. Hsuan, M. Bitter, C.K. Phillips, J.R. Wilson, C. Bush, H.H. Duong, D. Darrow, G.W. Hammett, K.W. Hill, R.P. Majeski, S. Medley, M. Petrov, E. Synakowski, M. Zarnstorff, S. Zweben, ICH-induced plasma rotation on TFTR, in: Proceedings of the 11th International Conference on the Application of RF Power to Plasmas, Palm Springs, 1995.

[22] S. Wukitch, C. Litwin, M. Harper, R. Parker, N. Hershkowitz, Experimental observation of RF driven plasma flow in the phaedrus-T tokamak, Phys. Rev. Lett. 77 (1996) 294.

[23] F. Najmabadi and the ARIES Team, The ARIES-I Tokamak Reactor Study—Final Report, University of California, Los Angeles, report UCLA-PPG-1323, vol. 2, 1991.

[24] F. Najmabadi, R.W. Conn and the ARIES Team, The ARIES-II and -IV Second Stability Tokamak Fusion Power Plant Study, The Final Report, UCLA Report, UCLA-PPG-1461 (to be published); also F. Najmabadi, R.W. Conn, et al., Directions for Attractive Tokamak Reactors: The ARIES-II and ARIES-IV Second Stability

Designs, Proc. 14th Int. Conf. on Plasma Physics and Control. Nuc. Fus. Res., Wurzburg, Germany (October 1992), IAEA, Vienna (1993) 295.
[25] D.A. Ehst, Fast Wave Current Drive: Experimental Status and Reactor Prospects, Argonne National Laboratory, report ANL/FPP/TM-219, 1988.
[26] M. Ono, High Harmonic Fast Waves in High Beta Plasmas, Princeton Plasma Physics Laboratory, report PPPL-3091, 1995.
[27] T.K. Mau, D.A. Ehst, S.C. Jardin, C.E. Kessel, B.J. Lee, The Aries Team, Plasma system requirements and performance data base for the starlite/demo fusion power plant, in: Proceedings of the 16th IEEE/NPSS Symposium on Fusion Engineering, Urbana, IL, vol. 2, 1995, p. 1194.
[28] T.K. Mau, S.S. Chiu, R.W. Harvey, Modelling of fast-wave current drive in standard and second-stability bootstrapped reactor plasmas, in: EPS Topical Conference Abstracts on Radiofrequency Heating and Current Drive of Fusion Devices, Brussels, 1992, p. 181.
[29] D.A. Ehst, C.F.F. Karney, Approximate formula for radio-frequency current drive efficiency with magnetic trapping, Nucl. Fusion 31 (1991) 1933.
[30] T.K. Mau, Starlite Physics Team, Current drive studies for starlite/demo powerplants, Bull. Am. Phys. Soc. 40 (1995) 1703.
[31] S.C. Chiu, C.F.F. Karney, T.K. Mau, Y.R. Lin-Liu, Theory of current drive by parallel acceleration of electrons in a weakly relativistic plasma, Phys. Plasmas 2 (1995) 450.
[32] L. Barr, B.G. Logan, A slot divertor for tokamaks with high divertor heat loads, Fusion Tech. 18 (1990) 251.
[33] K.A. Werley, Tokamak and RFP ignition requirements, in: Proceedings of the 14th IEEE Symposium on Fusion Engineering, San Diego, CA, vol. 1, 30 September–3 October, 1991, p. 416.
[34] D.E. Post, K. Borrass, J.D. Callen, S.A. Cohen, J.G. Cordey, F. Engelmann, ITER Physics, International Thermonuclear Experimental Reactor documentation series No. 21, November, 1990.
[35] D.E. Post, R.V. Jensen, C.B. Tarter, W.H. Grasberger, W.A. Lokke, Steady-state radiative cooling rates for low-density, high-temperature plasma, At. Data Nucl. Data Tables 20 (1977) 397.
[36] D.L. Hillis, K.H. Finken, J.T. Hogan, K.H. Dippel, R.A. Moyer, A. Pospieszczyk, D. Rusbuldt, K. Akaishi, R.W. Conn, H. Euringer, D.S. Gray, L.D. Horton, R.A. Hulse, R.C. Isler, C.C. Klepper, P.K. Mioduszewski, A. Miyahara, G.H. Wolf, Helium exhaust and transport studies with the ALT-II pump limiter in the TEXTOR tokamak, Phys. Rev. Lett. 65 (1990) 2382.
[37] M.R. Wade, D.L. Hillis, J.T. Hogan, R. Maingi, M.M. Menon, M.A. Mahdavi, W.D. West, K.H. Burrell, P. Gohil, R.J. Groebner, R.-M. Hong, D.H. Kellman, J.C. Phillips, R.P. Seraydarian, The DIII-D Team, D.F. Finkenthal, Helium transport and exhaust studies in enhanced confinement regimes in DIII-D, Phys. Plasmas 2 (1995) 2357.
[38] U. Samm, H.L. Bay, P. Bogen, H. Hartwig, E. Hintz, K. Hothker, Y.T. Lie, A. Pospieszczyk, G.G. Ross, D. Rusbuldt, B. Schweer, Plasma edge research on TEXTOR, Plasma Phys. Control. Fusion 29 (1987) 1321.
[39] R.J. Goldston, Physics of the steady-state advanced tokamak, Phys. Plasmas 3 (1996) 1794.
[40] P.B. Parks, R.J. Turbull, C.A. Foster, A model for the ablation rate of a solid hydrogen pellet in a plasma, Nucl. Fusion 17 (1977) 539.
[41] Presentation by the ITER Director to the Fourth Meeting of the Technical Advisory Committee, ITER/TAC-IV, vol. 1, 1994.
[42] D. Post, J. Abdallah, R.E.H. Clark, N. Putvinskaya, Calculation of energy losses due to atomic processes in tokamak with applications to the ITER divertor, Phys. Plasmas 2 (1995) 2328.
[43] ITER EDA Newsletter, vol. 4, No. 9, IAEA, Vienna, 1995.
[44] C.E. Bush, S.A. Sabbagh, S.J. Zweben, R.E. Bell, E.J. Synakowski, G. Taylor, S. Batha, M. Bell, M. Bitter, N.L. Bretz, R. Budny, Z. Chang, D.S. Darrow, P.C. Efthimion, D. Ernst, E. Fredrickson, G.R. Hanson, L.C. Johnson, J. Kesner, B. Le Blanc, F.M. Levinton, D. Mansfield, M.E. Mauel, E. Mazzucato, D. McCune, M. Murakami, R. Nazikian, G.A. Nauratil, H. Park, S.F. Paul, C.K. Phillips, M.H. Redi, J. Schivell, S.D. Scott, C.H. Skinner, H.H. Towner, J.B. Wilgen, M.C. Zarnstorff, TFTR Group, Deuterium-tritium high confinement (H-mode) studies in the tokamak fusion test reactor, Phys. Plasmas 2 (1995) 2366.
[45] J.A. Snipes, R.L. Boivin, C. Christensen, C. Fiore, D. Garnier, J. Goetz, S.N. Golovato, M. Graf, R.S. Granetz, M. Greenwald, A. Hubbard, I.H. Hutchinson, J. Irby, B. LaBombard, E.S. Marmar, A. Niemczewski, P. O'Shea, M. Porkolab, P. Slek, Y. Takase, J.L. Terry, M. Umansky, S.M. Wolfe, Characteristics of high confinement modes in alcator C-Mod, Phys. Plasmas 3 (1996) 1992.
[46] D.A. Ehst, A. Hassanein, Thermal ablation of plasma facing surfaces in tokamak disruptions: sensitivity to particle kinetic energy, ANL/FPP/TM-289, 1996.
[47] H. Madarame, T. Sukegawa, K. Okamoto, A simulated plasma disruption experiment using magneto–plasma–dynamic arcjet, Fusion Eng. Des. 18 (1991) 109.
[48] V.N. Litunovsky, I.B. Ovchinnikov, A.A. Drozdov, V.E. Kuznetsov, B.V. Ljublin, V.A. Titov, Study of material response on simulated ITER disruptive plasma heat load with variable duration, in: Proceedings of the 16th Symposium on Fusion Engineering, 1995, p. 435.
[49] F. Najmabadi, R.W. Conn and the ARIES Team, The PULSAR Study—A Pulsed Tokamak Fusion Power Plant, University of California, San Diego, Report UCSD-ENG-003 (1997).